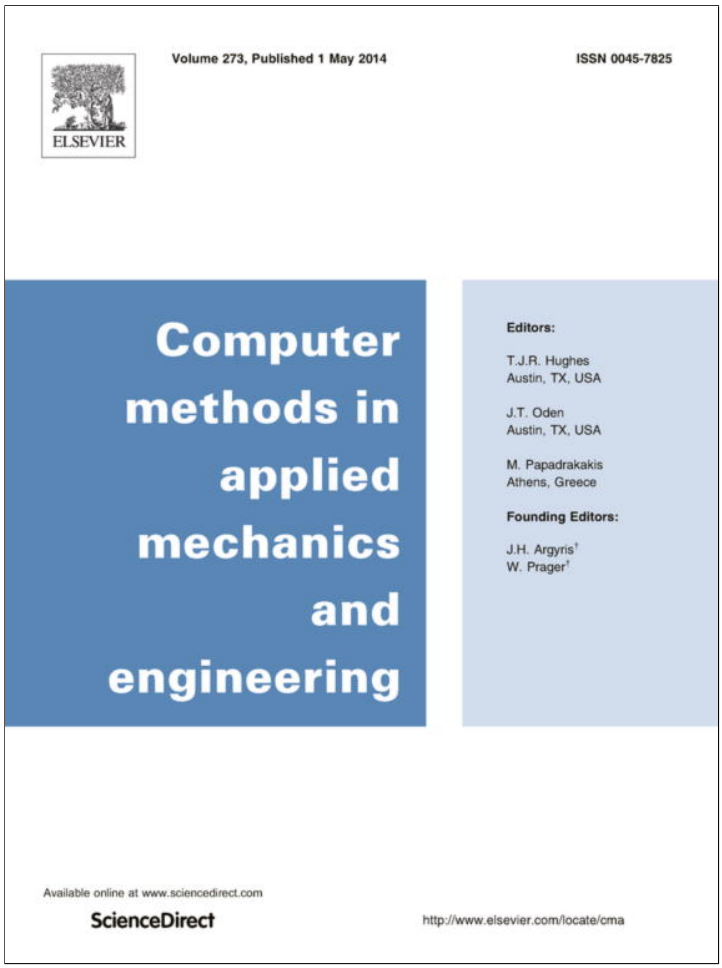

Comput. Methods Appl. Mech. Engrg. 273 (2014) 273–302

Contents lists available at ScienceDirect

Comput. Methods Appl. Mech. Engrg.

journal homepage: www.elsevier.com/locate/cma

Multiscale modeling and simulation of dynamic wetting

Hiroyuki Minaki [a], Shaofan Li [b,*]

[a] Department of Mechanical Engineering, University of California, Berkeley, CA 94720, USA
[b] Department of Civil and Environmental Engineering, University of California, Berkeley, CA 94720, USA

ARTICLE INFO

Article history:
Received 3 June 2013
Received in revised form 25 January 2014
Accepted 31 January 2014
Available online 13 February 2014

Keywords:
Droplet spreading
Finite element analysis
Moving contact line theory
Surface tension
Wettability
Young's equation

ABSTRACT

In this paper, we present a multiscale analysis on dynamic wetting and liquid droplet spreading on solid substrates. In the proposed multiscale dynamic wetting model, we couple molecular scale adhesive interaction (the van der Waals type force) and the macro-scale flow – that is: we combine a coarse-grain adhesive contact model with a modified Gurtin–Murdoch surface elasto-dynamics theory to formulate a multiscale moving contact line theory to simulate dynamic wetting. The advantage of adopting the coarse grain adhesive contact model in the moving contact line theory is that it can levitate and separate the liquid droplet with the solid substrate, so that the proposed multiscale moving contact line theory avoids imposing the non-slip condition, and then it removes the subsequent singularity problem, which allows the surface energy difference and surface stress propelling droplet spreading naturally.

By employing the proposed method, we have successfully simulated droplet spreading over various elastic substrates. The obtained numerical simulation results compare well with the experimental and molecular dynamics results reported in the literature.

1. Introduction

Wetting or droplet spreading on a solid substrate is an interesting and fascinating phenomenon in colloidal science that has many important applications in the fields of soft matter physics, chemistry, biology, and engineering, for example, cell motility, self-cleaning biological systems, wet friction between tire and pavement, pharmaceutical drugs manufacturing and delivery system, consumer electronics, e.g. hard disk drive, various bio- and soft matter sensors, etc.

In chemical physics, wetting is a physical process of liquid and gas phases concurrently interacting with the surface of a solid phase, resulting from intermolecular interactions of a triple phase system when the three are brought together. The degree of wetting is referred to as wettability, which is determined by the intermolecular force balance between adhesive, cohesive, and other contact forces. Wetting and the related surface tension and surface energy effects that control wetting are also responsible for other related physical phenomena, such as droplet spreading, capillary effect, surfactant assembly, wet friction, etc.

Because of vast applications and potential transformative impact, there is a long history and large body literature of attempting to establish a numerical method to simulate wetting and droplet spreading process at macroscale, e.g. [25,33,22,9,10,12,14] to name a few. Among them, the most notable one is the so-called moving contact line hydrodynamics theory [11,48,37,28]. However, there has been an outstanding challenge in the conventional moving contact-line

* Corresponding author.
E-mail address: shaofan@berkeley.edu (S. Li).

http://dx.doi.org/10.1016/j.cma.2014.01.030
0045-7825/

hydrodynamics theory: a key technical ingredient of the moving contact line hydrodynamics is the non-slip boundary condition along the liquid/solid interface, which will lead to singularity in shear stress distribution at the front of the moving contact line between the liquid and solid phase (see Fig. 1 (a) and [51] for detailed discussion). In turn, the singular shear stress on the droplet will force the liquid droplet moving along the interface, which then violates the a priori assumption of non-slip condition. This technical difficulty has posted great challenge for macroscale simulation of dynamic wetting and droplet spreading.

In this work, we propose a multiscale dynamic wetting model (MDWM) that combines the conventional hydrodynamic contact line theory [11,48,37,28] and a modified Gurtin–Murdoch surface elasticity theory [16,17] with the coarse grain adhesive contact model developed by Sauer and Li [38–41], so that the droplet is levitated above the solid substrate (see Fig. 1(b)). In doing so, it completely eliminates singularity problem of the conventional hydrodynamic contact line theory (see recent discussions in [51]), while retaining the surface energy description in dynamics wetting modeling. To understand how the proposed method works, we have done a comparison simulation by using the conventional moving contact line method and MDWM method proposed in the work (see Fig. 1). In the moving contact line hydrodynamics simulation, a singular shear stress arises due to the fact that the initial contact line front between the liquid phase and solid phase forms a crack shaped cleavage (see Fig. 1(a)), and the abrupt change of surface tangent direction will cause stress concentration. On the other hand, if one can levitate the liquid droplet over the solid substrate, and it will separate the liquid phase and solid phase, i.e. creating a gap between the solid surface and liquid surface, as what really happens in reality. By doing so, the mechanical or mathematical modeling induced pathology will naturally go away, which is one of the main motivations and contributions of this work.

To accomplish this goal, in this work we have proposed a multiscale dynamic wetting model, and have established its finite element formulation, and have carried out several numerical simulations. The paper is organized into eight sections. We begin in Section 2 by setting forth the multiscale dynamic wetting model (MDWM) in terms of its mathematical strong form, and subsequently in Section 3, we state and derive the Galerkin weak formulation of MDWM theory. With these preparations, we discuss finite element discretization and implementations of MDWM in Section 4. In Section 5, we discuss a special but important case of moving contact line theory, in which the surface stress is assumed to be constant in each surface element; and in Section 6, we discuss the general surface contact line theory, in which the surface stress is non-uniform. In Section 7, several numerical examples are presented, and finally in Section 8, we conclude the presentation by assessing the advantages and limitations of the proposed MDWM model.

2. Multiscale dynamic and wetting model (MDWM)

We consider a general triple phase system of gas, liquid, and solid phase as shown in Fig. 2, in which $\Omega_\alpha,\ \alpha = G, L,$ and S are the bulk volumes for gas (G), liquid (L), and solid (S) phases. One can see from Fig. 1. that along each interphase, there are two surfaces. For example, Γ_{GL} is the gas surface of the gas–liquid interphase, whereas Γ_{LG} is the liquid surface of the gas–liquid interphase (see the order of letter G and L). By the same convention, we denote that Γ_{LS} is the liquid surface of the liquid–solid interphase, whereas Γ_{SL} is the solid surface of the liquid–solid interphase; Γ_{GS} is the gas surface of the gas–solid interphase, whereas Γ_{SG} is the solid surface of the gas–solid interphase. For the triple system configuration shown in Fig. 2, we have $\partial\Omega_L = \Gamma_{LG} \cup \Gamma_{LS}$, $\partial\Omega_S = \Gamma_{SL} \cup \Gamma_{SG}$, and $\partial\Omega_G = \Gamma_{GL} \cup \Gamma_{GS}$.

As a hybrid multiscale model, we model the bulk medium by using continuum mechanics formulations, i.e.

$$\frac{\partial \boldsymbol{\sigma}_\alpha}{\partial \mathbf{x}} + \rho_\alpha \mathbf{b}_\alpha = \rho_\alpha \ddot{\mathbf{u}}_\alpha, \quad \alpha = G, L, \text{ and } S \tag{1}$$

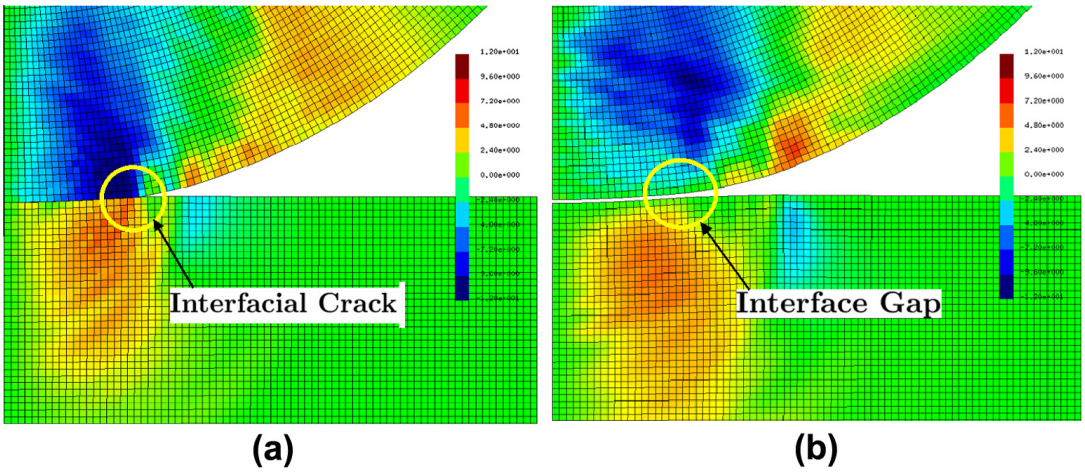

Fig. 1. Comparison simulation results of (a) Singularity in shear stress (σ_{12}) distribution obtained from the moving contact line hydrodynamics simulation, and (a) shear stress (σ_{12}) distribution from a MDWM simulation of adhesive contact and droplet spreading.

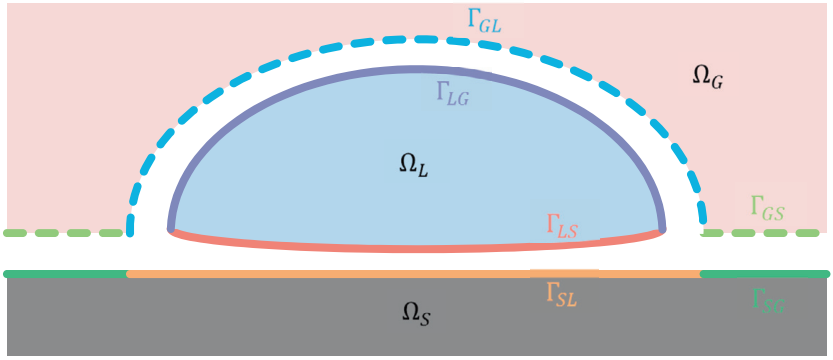

Fig. 2. Schematic illustrate of the triple phase system.

where $\boldsymbol{\sigma}_\alpha$ are the Cauchy stresses in each phase; ρ_α are the mass densities per unit volume in each phase; $\mathbf{b}_\alpha$ are the body forces per unit mass in each phase, and $\mathbf{u}_\alpha$ are the displacement fields in each phase. Since the stress in the gas phase is negligible, and we only consider the equation of motion in $\alpha = L$ and S.

Inside three interphases and adjacent bulk media, we consider the small scale adhesive contact force, which has been described in a number of mesoscale contact models, such as the JKR theory [23] or the DMT theory [8], and the recent coarse-grained adhesive contact model e.g. [38–41]. In the coarse-grained adhesive contact model, the small scale adhesive interaction between two adjacent continua is described by the long-range van der Waals type of molecular interaction during the contact.

The inter-continuum interaction is then homogenized so that it may be represented by a continuum interaction energy. By the homogenization of the intersolid potential utilizing the Cauchy–Born rule, a continuous interaction energy that surrounds each body is obtained. Fig. 3 illustrates the kinematic description of two interacting bodies in the framework of adhesive continuum mechanics. The bodies are denoted by $\mathbf{r}_1 \in \Omega_1$ and $\mathbf{r}_2 \in \Omega_2$ in the current configuration, β_1 and β_2 are the atom densities, and r is the distance between two points. Along the interphase of the two bodies, the inter-solid adhesive energy density from body one to body two may be written as

$$W_{1\to 2}(\mathbf{r}_2) = \frac{1}{2}\int_{\Omega_1} \beta_1 \phi(|\mathbf{r}_1 - \mathbf{r}_2|) dv_1, \quad \text{where} \quad \mathbf{r}_2 \in \Omega_2,\ \mathbf{r}_1 \in \Omega_1.$$

where β_1 is the atom or molecule density in body one, and ϕ is the atomistic or molecular potential that determines the force field between atoms or molecules in the body one and body two, and $\Omega_i,\ i = 1, 2$ are the volumes for body one or body two.

Note that the atom density β_1 is often referred to as the inverse of volume of the Wigner–Seitz cell (the primitive unit cell) for crystalline solids, if the unit cell has only one atom. Similarly, we have

$$W_{2\to 1}(\mathbf{r}_1) = \frac{1}{2}\int_{\Omega_2} \beta_2 \phi(|\mathbf{r}_1 - \mathbf{r}_2|) dv_2, \quad \text{where} \quad \mathbf{r}_2 \in \Omega_2,\ \mathbf{r}_1 \in \Omega_1.$$

where β_2 is the atom or molecule density in body two. Therefore, the total interaction energy Π^C for the two interacting bodies may be written as

$$\Pi^C = \int_{\Omega_1}\int_{\Omega_2} \beta_1\beta_2 \phi(r) dv_2\, dv_1, \tag{2}$$

where $\phi(r)$ is the interatomic potential, and in simulations we often use the Lennard–Jones potential as the interatomic potential to model the van der Waals type of adhesive force,

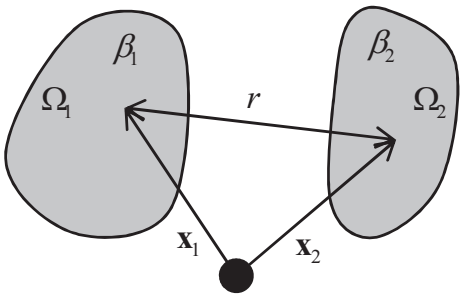

Fig. 3. The kinematics of two interacting bodies.

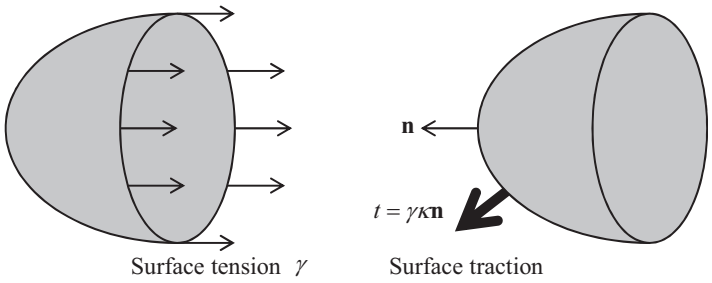

Fig. 4. The surface traction in terms of the surface tension.

$$\phi(r) = \epsilon\left(\frac{r_0}{r}\right)^{12} - 2\epsilon\left(\frac{r_0}{r}\right)^{6}, \tag{3}$$

where the first term is the contribution of the repulsion when two atoms come close, and the second term is the contribution of the van der Waals force; ϵ is the depth of the potential well, r_0 is the equilibrium distance, and r is the distance between two atoms.

In principle, the coarse grain adhesive contact model should automatically take into account the surface tension effect in different continuum media. However, if we do not or could not adopt atomistic enriched constitutive relation in continuum formulation such as the surface Cauchy–Born model [34,35], which is very difficult to do for a liquid phase, the surface tension effect may not be captured by a coarse-grained inter-continuum interaction.

To amend such shortcoming, we include additional continuum surface description, i.e. a set of surface dynamic equations that are similar to the Gurtin–Murdoch interface formulation [16–18], to supplement surface energy information along different interphase contact lines. In specific, we consider the following equations of motions on the gas, liquid, and solid surfaces,

$$\mathbf{f}^{D,\alpha} := \nabla_s \boldsymbol{\varsigma}_\alpha + \mathbf{t}_\alpha = \rho_{s\alpha}\mathbf{a}_\alpha, \quad \alpha = G, L, S \tag{4}$$

where $\rho_{s\alpha}$ are the surface mass densities, and ∇_s is the surface gradient operator that is defined as

$$\nabla_s := \nabla - \mathbf{n}(\mathbf{n}\cdot\nabla), \tag{5}$$

where $\mathbf{n}$ is the out-normal of the surface tangent plane. The surface stresses of the triple system are denoted as $\boldsymbol{\varsigma}_\alpha,\ \alpha = G, L, S$, and $\mathbf{t}_\alpha,\ \alpha = G, L, S$ are traction vectors on the surfaces of the different phases, and $\mathbf{a}_\alpha$ are surface acceleration at surface material points.

Different from the Gurtin–Murdoch (GM) theory [16,18], in this work we are dealing with some supplement *surface* conditions rather than *the interface conditions* as those in GM theory. This is because we assume that between any of two distinct phases of the triple phase system there is an interphase; and at the two sides of the interphase there are two distinct surfaces. Second, in the Gurtin–Murdoch theory, the traction is defined as

$$\mathbf{t}_\alpha = \boldsymbol{\sigma}_\alpha \cdot \mathbf{n}_\alpha,$$

where $\boldsymbol{\sigma}_\alpha$ are the Cauchy stress in bulk media (phase). In the proposed MDWM theory, the traction force on the liquid–solid interface may be taken as the projection of the adhesive force derived from CGCM theory, i.e.

$$\mathbf{t}_\alpha = \mathrm{Proj}_\alpha[\mathbf{f}^{adh}] = \mathbf{t}_\alpha^{adh} = f(s)(\mathbf{E}\cdot\mathbf{n}_\alpha)\mathbf{E}, \quad \alpha = LS, SL,$$

where s is the distance of the surface separation at where the traction is measured, $f(\cdot)$ is the specified function depending on coarse grained adhesive potential, $\mathbf{E}$ is a vector depending on contact morphology, and $\mathbf{n}_\alpha$ is the out-normal of the α-th surface. The above surface traction can be calculated by using the well-known Derjaguin approximation technique [6], in which $\mathbf{E}$ is unspecified and problem-dependent. The latest improvements and variants of the Derjaguin approximation, e.g. [7], provide detailed procedure to calculate adhesive surface traction, i.e. the terms $\mathbf{E}$ and $f(s)$, for given adhesive potential and contact surface morphology. By doing so, the multiscale dynamic wetting model is made consistent or compatible with the coarse-grain adhesive contact model.

In contrast with the original Gurtin–Murdoch theory of *elastostatic interface*, in this work we must consider the inertial effect because we study the phenomenon of dynamic wetting. The inertial effect is represented by the terms, $\mathbf{f}^{D,\alpha},\ \alpha = G, L, S$, which are the D'Alembert force densities on different surfaces. In this work, we postulate that the surface D'Alembert force densities equals

$$\rho_{s\alpha}\mathbf{a}_\alpha, \quad \alpha = G, L, S, \tag{6}$$

where $\rho_{s\alpha}$ is the surface mass density of α phase, and $\mathbf{a}_\alpha$ is surface acceleration of α phase. The surface D'Alembert force density has the unit (N/m^2), and the traction $\mathbf{t}_\alpha,\ \alpha = G, L, S$, have the same unit (N/m^2), whereas the unit for the surface stresses,

ς_α, $\alpha = G, L, S$, is (N/m). To focus on the dynamic wetting and droplet spreading problem, we make the following assumptions:

2.1. Surface kinematic assumptions

A1. We assume that the stiffness of solid phase is much larger than that of liquid or gas phases, so that the magnitude of velocity of the surface particle on the solid phase is much smaller than that of the surface particle on the liquid or gas phase that shares the same interphase, i.e.

$$|\mathbf{a}_S| \ll |\mathbf{a}_L| \;\rightarrow\; |\rho_{sS}\mathbf{a}_S| \ll 1.$$

A2. We assume that the surface particle acceleration on the gaseous phase is at the same order of magnitude of that of the liquid phase; and because the mass density in the gaseous phase is much smaller than that of the liquid phase, we have

$$|\mathbf{a}_G| \sim |\mathbf{a}_L| \quad \text{such that} \quad |\rho_{sG}\mathbf{a}_G| \ll 1 \quad (\rho_{sG} \ll \rho_{sL}).$$

These assumptions simplify Eq. (4) to following forms,

$$0 = \nabla_s \boldsymbol{\varsigma}_G + \mathrm{Proj}_G[\mathbf{f}^{adh}], \quad \forall \mathbf{x} \in \partial\Omega_G, \tag{7}$$

$$\mathbf{f}^{D,L} = \nabla_s \boldsymbol{\varsigma}_L + \mathrm{Proj}_L[\mathbf{f}^{adh}], \quad \forall \mathbf{x} \in \partial\Omega_L, \tag{8}$$

$$0 = \nabla_s \boldsymbol{\varsigma}_S + \mathrm{Proj}_S[\mathbf{f}^{adh}], \quad \forall \mathbf{x} \in \partial\Omega_S, \tag{9}$$

which govern the continuum surface equilibrium of the triple system under dynamic motions. In computations, we have used the following formulas to calculate the surface stress,

$$\boldsymbol{\varsigma}_G = \gamma_G \mathbf{I}_s^{(2)}, \tag{10}$$

$$\boldsymbol{\varsigma}_L = \gamma_L \mathbf{I}_s^{(2)} + \nabla_s \gamma_L, \tag{11}$$

$$\boldsymbol{\varsigma}_S = \gamma_S \mathbf{I}_s^{(2)} + \frac{\partial \Gamma_S}{\partial \boldsymbol{\epsilon}_s} + \gamma_S \nabla_s \otimes \mathbf{u}, \tag{12}$$

where γ_S, γ_L and γ_S are the surface tension in different phases; Γ_S is the solid surface strain energy; $\boldsymbol{\epsilon}_s$ is the surface strain tension; ∇_s is the surface gradient operator defined in (5); and the operator $\otimes$ is the standard notation for tensor product in tensor algebra or analysis e.g. in [44]. Note that $\mathbf{I}_s^{(2)}$ denotes the unit tensor on a smooth surface or two-dimensional manifold, which is defined as [26],

$$\mathbf{I}_s^{(2)} := \mathbf{P}\mathbf{I} = \mathbf{P}, \tag{13}$$

where $\mathbf{I}$ is the unit tensor in a three-dimensional Euclidean space, and $\mathbf{P}$ is the projection tensor defined as,

$$\mathbf{P} := \mathbf{I} - \mathbf{n} \otimes \mathbf{n},$$

where $\mathbf{n}$ is the out-normal of the surface at the point of interesting. In some part of the text, in order to emphasize the material properties of the manifold, we write it as $\mathbf{I}_s^{(\alpha)}$, $\alpha = G, L, S$ or LS, GS and LG etc. in a manner that is self-evidence.

If the solid surface is the surface of a crystalline solid, one may also use the Surface Cauchy–Born model [34,35] with the atomistic potential of the crystal to derive both surface energy as well as surface stress $\boldsymbol{\varsigma}^S$. In fact, we have calculated surface energy by using the surface Cauchy–Born model in one example in Section 7.

For example, if we consider a equilibrium state of gas–liquid interface, we may let

$$\mathbf{f}^{D,L} = 0, \quad \mathrm{Proj}_G[\mathbf{f}^{adh}] = -\boldsymbol{\sigma}_G \cdot \mathbf{n} = +p_G \mathbf{n}$$

and

$$\mathrm{Proj}_L[\mathbf{f}^{adh}] = \boldsymbol{\sigma}_L \cdot \mathbf{n} = -p_L \mathbf{n},$$

$$\nabla_s \boldsymbol{\varsigma}_G + p_G \mathbf{n} = 0, \quad \forall \mathbf{x} \in \partial\Omega_G, \tag{14}$$

$$\nabla_s \boldsymbol{\varsigma}_L - p_L \mathbf{n} = 0, \quad \forall \mathbf{x} \in \partial\Omega_L. \tag{15}$$

Without loss generality, we may choose $\boldsymbol{\varsigma}_G = \gamma_G \mathbf{I}_s^{(2)}$ and $\boldsymbol{\varsigma}_L = \gamma_L \mathbf{I}_s^{(2)}$. Recall $\mathbf{I}_s = \mathbf{P}\mathbf{I} = \mathbf{P}$, $\nabla_s = \nabla - \mathbf{n}(\mathbf{n} \cdot \nabla)$, and $\mathbf{P} = \mathbf{I} - \mathbf{n} \otimes \mathbf{n}$ is the projection operator. Subsequently, one can readily show that

$$\nabla_s \mathbf{I}_s^{(2)} = \nabla_s \mathbf{P} = 2\kappa \mathbf{n},$$

where κ is the average curvature of the surface.

Adding Eqs. (14) and (15) together and considering that liquid and gas surfaces have the same curvature when they form a same interface, we have

$$\nabla_s(\varsigma_G+\varsigma_L)+(p_G-p_L)\mathbf{n}=0,\quad \rightarrow p_L-p_G=2(\gamma_G+\gamma_L)\kappa=2\gamma_{LG}\kappa,$$

which is the standard Young–Laplace equation of the gas–liquid interphase. Alternatively, we may write

$$[\mathbf{t}]_{LG}:=\nabla_s(\varsigma_G+\varsigma_L)\ \rightarrow [\mathbf{t}]_{LG}=-2\gamma_{LG}\kappa\mathbf{n}. \tag{16}$$

This equation may be extended to the liquid–solid surface, if we take the following approximation,

$$\varsigma_S=\gamma_S\mathbf{I}_s^{(2)}+\frac{\partial\Gamma_S}{\partial\epsilon_s}+\gamma_S\nabla_s\otimes\mathbf{u}\approx\gamma_S\mathbf{I}_s^{(2)},$$

which leads to

$$[\mathbf{t}]_{LS}:=\nabla_s(\varsigma_S+\varsigma_L)\ \rightarrow [\mathbf{t}]_{LS}=-2\gamma_{LS}\kappa\mathbf{n}, \tag{17}$$

which is the formula used in standard text book of colloidal physics or chemistry.

3. Galerkin weak formulation of MDWM

In this Section, we discuss the Galerkin weak formulation of the multiscale dynamic wetting model.

We consider a triple system with negligible gas phase energy transfer. The total Lagrange of the system may be written as

$$\mathcal{L}=\sum_{\alpha=L,S}\left[T_\alpha-(\Pi_\alpha^{int}-\Pi_\alpha^{ext})\right]-\Pi^C,\quad\text{and}\quad \mathcal{S}=\int_{t_1}^{t_2}L dt, \tag{18}$$

where $\alpha=L,S$ denotes the liquid and solid phases, T_α are the kinetic energies, Π_α^{int} are the internal energies, and Π_α^{ext} are the external energies.

Considering the least action or the stationary action principle, $\delta\mathcal{S}=0$, we have

$$\delta\mathcal{S}=\int_{t_1}^{t_2}\delta\mathcal{L}dt=\int_{t_1}^{t_2}\left\{\sum_{\alpha=L,S}\left[\delta T_\alpha-(\delta\Pi_\alpha^{int}-\delta\Pi_\alpha^{ext})\right]-\delta\Pi^C\right\}dt=0,$$

$\forall\delta\mathbf{u}_L,\delta\mathbf{u}_S\in H^1(\Omega_L)\cup H^1(\Omega_S)$, where $\delta\mathbf{u}_L$ and $\delta\mathbf{u}_S$ are the variations of displacements in the liquid and solid phases. The variation of the kinetic energy is given by

$$\delta T_\alpha=\int_{\Omega_\alpha}\rho_\alpha\dot{\mathbf{u}}_\alpha\cdot\delta\dot{\mathbf{u}}_\alpha dv_\alpha,\quad \alpha=L,S; \tag{19}$$

where ρ_α are the mass densities in the current configuration. The variation of the internal energy is given by

$$\delta\Pi_\alpha^{int}=\int_{\Omega_\alpha}\boldsymbol{\sigma}_\alpha:\frac{\partial\delta\mathbf{u}_\alpha}{\partial\mathbf{x}}dv_\alpha,\quad \alpha=L,S. \tag{20}$$

The variation of the external energy is given as

$$\delta\Pi_\alpha^{ext}=\int_{\Omega_\alpha}\rho_\alpha\mathbf{b}_\alpha\cdot\delta\mathbf{u}_\alpha dv+\int_{\partial\Omega_\alpha}\mathbf{f}^{D,\alpha}\cdot\delta\mathbf{u}_\alpha ds,\quad \alpha=L,S, \tag{21}$$

where $\mathbf{b}_\alpha$ are the body forces, and $\mathbf{t}_\alpha$ are the surface tractions. Since we assume that $\mathbf{f}^{D,G}=0$, we may rewrite the total external virtual work as,

$$\delta\Pi^{ext}=\int_{\Omega_L}\rho_L\mathbf{b}_L\cdot\delta\mathbf{u}_L dv+\int_{\Omega_S}\rho_S\mathbf{b}_S\cdot\delta\mathbf{u}_S dv+\int_{\partial\Omega_G}\mathbf{f}^{D,G}\cdot\delta\mathbf{u}_G ds+\int_{\partial\Omega_L}\mathbf{f}^{D,L}\cdot\delta\mathbf{u}_L ds+\int_{\partial\Omega_S}\mathbf{f}^{D,S}\cdot\delta\mathbf{u}_S ds. \tag{22}$$

The variation of the interaction energy is given by

$$\delta\Pi^C=\int_{\Omega_L}\int_{\Omega_S}\beta_L\beta_S\left(\frac{\partial\phi(r)}{\partial\mathbf{x}_L}\cdot\delta\mathbf{u}_L+\frac{\partial\phi(r)}{\partial\mathbf{x}_S}\cdot\delta\mathbf{u}_S\right)dv_S dv_L. \tag{23}$$

Finally we can obtain following variational equations,

$$\begin{aligned}\int_{t_1}^{t_2}\Bigg\{&\sum_{\alpha=L,S}\left[\int_{\Omega_\alpha}\rho\mathbf{v}_\alpha\cdot\delta\dot{\mathbf{u}}_\alpha dv-\int_{\Omega_\alpha}\boldsymbol{\sigma}_\alpha:\frac{\partial\delta\mathbf{u}_\alpha}{\partial\mathbf{x}_\alpha}dv+\int_{\Omega_\alpha}\rho_\alpha\mathbf{b}_\alpha\cdot\delta\mathbf{u}_\alpha dv+\int_{\partial\Omega_\alpha}\mathbf{f}^{D,\alpha}\cdot\delta\mathbf{u}_\alpha ds\right]+\int_{\partial\Omega_G}\mathbf{f}^{D,G}\cdot\delta\mathbf{u}_G ds\\&-\int_{\Omega_L}\int_{\Omega_S}\beta_L\beta_S\left(\frac{\partial\phi(r)}{\partial\mathbf{x}_L}\cdot\delta\mathbf{u}_L+\frac{\partial\phi(r)}{\partial\mathbf{x}_S}\cdot\delta\mathbf{u}_S\right)dv_S dv_L\Bigg\}dt=0,\quad\forall\delta\mathbf{u}_G,\delta\mathbf{u}_L,\delta\mathbf{u}_S.\end{aligned} \tag{24}$$

This is the Galerkin weak formulation of the multiscale dynamic wetting model. For finite element analysis and implementation of CGCM, readers may consult [38–41]. In this work, we shall focus on how to evaluate the virtual work due to surface tension, i.e. the terms,

$$\int_{\partial\Omega_\alpha} \mathbf{f}^{D,\alpha} \cdot \delta\mathbf{u}_\alpha ds, \quad \alpha = G, L, S,$$

where the superscript 'D' means that this is a dynamic force, and the superscript 'α' is the phase index.

In particular, we are interested in calculating the nodal surface tension force due to surface energy at the contact line as shown in Fig. 5. On the contact surface of the each phase, the following modified Gurtin–Murdoch type equations of motion are imposed, which are given as,

$$\mathbf{f}^{D,S} = \frac{\partial \boldsymbol{\varsigma}_S}{\partial \mathbf{x}} + \mathrm{Proj}_S[\mathbf{f}^{adh}], \tag{25}$$

$$\mathbf{f}^{D,L} = \frac{\partial \boldsymbol{\varsigma}_L}{\partial \mathbf{x}} + \mathrm{Proj}_L[\mathbf{f}^{adh}], \tag{26}$$

$$\mathbf{f}^{D,G} = \frac{\partial \boldsymbol{\varsigma}_G}{\partial \mathbf{x}} + \mathrm{Proj}_G[\mathbf{f}^{adh}], \tag{27}$$

where $\mathbf{f}^{D,S}$, $\mathbf{f}^{D,L}$, and $\mathbf{f}^{D,G}$ are the extra forces due to surface tension at the interfaces of triple system i.e. solid, liquid, and gas surface D'Alembert forces, and they have the unit (N/m^2); $\boldsymbol{\varsigma}_S$, $\boldsymbol{\varsigma}_L$, and $\boldsymbol{\varsigma}_G$ are the surface stress (N/m) with respect to different surfaces, and we can use projection operator to project the interphase adhesive force onto three different surfaces as well by denoting them as $\mathrm{Proj}_S[\mathbf{f}^{adh}]$, $\mathrm{Proj}_L[\mathbf{f}^{adh}]$, and $\mathrm{Proj}_G[\mathbf{f}^{adh}]$ where the subscript S, L and G denote solid, liquid, and gaseous surfaces, and the interphase adhesive force includes cohesive force as well as friction force (N/m^2).

Since the solid substrate is assumed to be much stiffer than the liquid phase, we neglect the effects of the surface inertia force on the solid surface, i.e. $\mathbf{f}^{D,S} \approx \mathbf{0}$ according to **Assumption 1**. Since the gaseous phase is much lighter than the liquid, based on **Assumption 2** we can neglect the surface inertia force on the gas surface as well, i.e. $\mathbf{f}^{D,G} \approx \mathbf{0}$.

The main task of MDWM finite element computation is to find the correct $\mathbf{f}^{D,L}$, so that the surface energy difference can drive droplet spreading. Let us first exam the external virtual work due to surface stress. In doing so, we first choose all the overlap surface virtual displacement as the same, i.e. $\delta\mathbf{u}_\alpha = \mathbf{w}$. We then have

$$\mathbf{0} = \int_{\partial\Omega_S} \mathbf{w} \cdot \frac{\partial \boldsymbol{\varsigma}_S}{\partial \mathbf{x}} ds + \int_{\partial\Omega_S} \mathbf{w} \cdot \mathrm{Proj}_S[\mathbf{f}^{adh}] ds, \tag{28}$$

$$\int_{\partial\Omega_L} \mathbf{w} \cdot \mathbf{f}^{D,L} ds = \int_{\partial\Omega_L} \mathbf{w} \cdot \frac{\partial \boldsymbol{\varsigma}_L}{\partial \mathbf{x}} ds + \int_{\partial\Omega_L} \mathbf{w} \cdot \mathrm{Proj}_L[\mathbf{f}^{adh}] ds, \tag{29}$$

$$\mathbf{0} = \int_{\partial\Omega_G} \mathbf{w} \cdot \frac{\partial \boldsymbol{\varsigma}_G}{\partial \mathbf{x}} ds + \int_{\partial\Omega_G} \mathbf{w} \cdot \mathrm{Proj}_G[\mathbf{f}^{adh}] ds, \tag{30}$$

where $\partial\Omega_S$, $\partial\Omega_L$ and $\partial\Omega_G$ denotes the solid, liquid, and gaseous surfaces. Consider $\partial\Omega_S = \Gamma_{SG} \cup \Gamma_{SL}$, $\partial\Omega_L = \Gamma_{LS} \cup \Gamma_{LG}$, and $\partial\Omega_G = \Gamma_{GS} \cup \Gamma_{GL}$. Integration by parts yields,

$$\mathbf{0} = -\int_{\Gamma_{SL}} \frac{\partial \mathbf{w}}{\partial \mathbf{x}} : \boldsymbol{\varsigma}_S ds - \int_{\Gamma_{SG}} \frac{\partial \mathbf{w}}{\partial \mathbf{x}} : \boldsymbol{\varsigma}_S ds + \int_{\Gamma_{SL}} \mathbf{w} \cdot \mathrm{Proj}_S[\mathbf{f}^{adh}] ds + \int_{\Gamma_{SG}} \mathbf{w} \cdot \mathrm{Proj}_S[\mathbf{f}^{adh}] ds, \tag{31}$$

$$\int_{\partial\Omega_L} \mathbf{w} \cdot \mathbf{f}^{D,L} ds = -\int_{\Gamma_{LS}} \frac{\partial \mathbf{w}}{\partial \mathbf{x}} : \boldsymbol{\varsigma}_L ds - \int_{\Gamma_{LG}} \frac{\partial \mathbf{w}}{\partial \mathbf{x}} : \boldsymbol{\varsigma}_L ds + \int_{\Gamma_{LS}} \mathbf{w} \cdot \mathrm{Proj}_L[\mathbf{f}^{adh}] ds + \int_{\Gamma_{LG}} \mathbf{w} \cdot \mathrm{Proj}_L[\mathbf{f}^{adh}] ds, \tag{32}$$

$$\mathbf{0} = -\int_{\Gamma_{GS}} \frac{\partial \mathbf{w}}{\partial \mathbf{x}} : \boldsymbol{\varsigma}_G ds - \int_{\Gamma_{GL}} \frac{\partial \mathbf{w}}{\partial \mathbf{x}} : \boldsymbol{\varsigma}_G ds + \int_{\Gamma_{GS}} \mathbf{w} \cdot \mathrm{Proj}_G[\mathbf{f}^{adh}] ds + \int_{\Gamma_{GL}} \mathbf{w} \cdot \mathrm{Proj}_G[\mathbf{f}^{adh}] ds, \tag{33}$$

In the above derivation, we have assumed that $\boldsymbol{\varsigma}_\alpha \mathbf{n}_\alpha = \mathbf{0}$ on $\partial\Omega_\alpha$, $\alpha = G, L, S$, in which $\mathbf{n}_\alpha$ are the normal vectors of the surface $\partial\Omega_\alpha$, $\alpha = S, L, G$. Here $\mathbf{f}^{D,L}$ is an inertia force on the liquid surface (N/m^2), and it is an unknown force vector that we are solving.

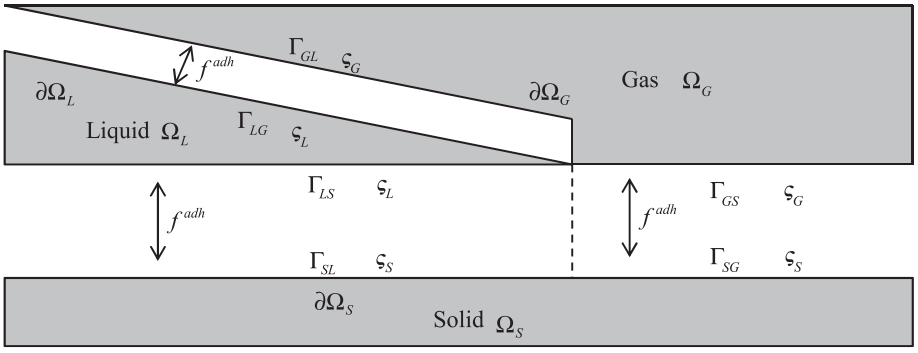

Fig. 5. Illustration of the contact line.

On Γ_{SL}, the projection of the adhesive force on the liquid surface, $\mathrm{Proj}_L[\mathbf{f}^{adh}]$, has the same magnitude but the opposite direction of the projection on the solid surface, i.e. $\mathrm{Proj}_L[\mathbf{f}^{adh}] = -\mathrm{Proj}_S[\mathbf{f}^{adh}]$. Similarly $\mathrm{Proj}_L[\mathbf{f}^{adh}] = -\mathrm{Proj}_G[\mathbf{f}^{adh}],\ \forall \mathbf{x} \in \Gamma_{LG}$, and $\mathrm{Proj}_S[\mathbf{f}^{adh}] = -\mathrm{Proj}_G[\mathbf{f}^{adh}],\ \forall \mathbf{x} \in \Gamma_{SG}$.

Adding Eqs. (31)–(33) together and utilizing the above relations between the projections of interface adhesive forces, we have

$$\int_{\partial\Omega_L} \mathbf{w}\cdot\mathbf{f}^{D,L} ds = -\int_{\Gamma_{SL}} \frac{\partial \mathbf{w}}{\partial \mathbf{x}} : (\varsigma_S + \varsigma_L) ds - \int_{\Gamma_{SG}} \frac{\partial \mathbf{w}}{\partial \mathbf{x}} : (\varsigma_S + \varsigma_G) ds - \int_{\Gamma_{LG}} \frac{\partial \mathbf{w}}{\partial \mathbf{x}} : (\varsigma_L + \varsigma_G) ds. \tag{34}$$

Note that we have used the fact that $\Gamma_{SG} = \Gamma_{GS}$, $\Gamma_{LG} = \Gamma_{GL}$, and $\Gamma_{SL} = \Gamma_{LS}$, where Γ^{SG} is interpreted as the solid side surface of a solid–gas interface, which equals to Γ_{GS} – the gas side surface of the same solid–gas interface. Similar interpretations may be made for Γ_{SL} and Γ_{LG}. Define

$$\varsigma_{LS} := \varsigma_S + \varsigma_L, \quad \forall \mathbf{x} \in \Gamma_{LS}, \tag{35}$$

$$\varsigma_{LG} := \varsigma_L + \varsigma_G, \quad \forall \mathbf{x} \in \Gamma_{LG}, \tag{36}$$

$$\varsigma_{SG} := \boldsymbol{\sigma}_S + \varsigma_G, \quad \forall \mathbf{x} \in \Gamma_{SG}. \tag{37}$$

Finally, the virtual work expression in terms of the surface stress of the triple system can be recast as follows,

$$\int_{\partial\Omega_L} \mathbf{w}\cdot\mathbf{f}^{D,L} ds = -\int_{\Gamma_{SG}} \frac{\partial \mathbf{w}}{\partial \mathbf{x}} : \varsigma_{SG} ds - \int_{\Gamma_{LS}} \frac{\partial \mathbf{w}}{\partial \mathbf{x}} : \varsigma_{LS} ds - \int_{\Gamma_{LG}} \frac{\partial \mathbf{w}}{\partial \mathbf{x}} : \varsigma_{LG} ds. \tag{38}$$

Eq. (38) is the weak form of the proposed dynamic wetting model along the interface contact line, which is a main result of MDWM. Since the gaseous phase and liquid phase are much softer than the solid phase, their *surface strain energy* (not surface energy!) may be negligible.

4. Finite element implementation

In continuum physics, surface tension, which is equivalent to surface energy in many cases, is applied onto the surface of contina [2,29,13,43]. In order to develop a multiscale computational method to solve dynamic wetting problem, we first introduce a finite element method-based surface tension model in this Section.

4.1. Finite element discrete equations of motion

Since our focus is on the droplet spreading, we first consider the Galerkin weak form for the liquid droplet,

$$\int_{\Omega_L} \rho_L \ddot{\mathbf{u}}\cdot\delta\mathbf{w} dv_L = -\int_{\Omega_L} \boldsymbol{\sigma} : \frac{\partial \mathbf{w}}{\partial \mathbf{x}} dv_L + \int_{\Omega_L} \rho_L \mathbf{b}_L \cdot \delta\mathbf{w} dv_L + \int_{\partial\Omega_L} \mathbf{f}^{D,L}\cdot\delta\mathbf{w} ds - \int_{\Omega_L}\int_{\Omega_S} \beta_L\beta_S \frac{\partial\phi(\mathbf{r})}{\partial \mathbf{x}_L}\cdot\mathbf{w} dv_S dv_L, \quad \forall \delta\mathbf{w} \in H^1(\Omega_L) \tag{39}$$

where $\mathbf{w}$ is the test function, which belongs the function space $H^1(\Omega_L)$ and satisfies homogeneous boundary condition on displacement boundary $\partial\Omega_L$. Eq. (39) is the Galerkin weak formulation of the multiscale dynamic wetting model.

We choose the following Bubnov–Galerkin finite element interpolation field in the bulk volume [1,21,52],

$$\mathbf{u}(\mathbf{x},t) = \sum_{I=1}^{N_{node}} N_I(\mathbf{x})\mathbf{d}_I(t), \tag{40}$$

$$\mathbf{w}(\mathbf{x},t) = \sum_{I=1}^{N_{node}} N_I(\mathbf{x})\mathbf{w}_I(t), \tag{41}$$

where N_{node} is the total number of finite element nodes, $N_I(\mathbf{x})$ are the Finite Element shape functions, $\mathbf{d}_I$ and $\mathbf{w}_I$ are the nodal displacement and the virtual displacement at node $I,\ I = 1, 2, \ldots N_{node}$.

Additionally we choose the following surface finite element interpolation field,

$$\mathbf{u}_s(\mathbf{x},t) = \sum_{I_s=1}^{N_{Snode}} N_{I_s}(\mathbf{x})\mathbf{d}_{I_s}(t), \tag{42}$$

$$\mathbf{w}_s(\mathbf{x},t) = \sum_{I_s=1}^{N_{Snode}} N_{I_s}(\mathbf{x})\mathbf{w}_{I_s}(t), \tag{43}$$

where N_{Snode} is the total number of surface element nodes, $N_{I_s}(\mathbf{x})$ are the surface finite element shape functions, $\mathbf{d}_{I_s}$ and $\mathbf{w}_{I_s}$ are surface nodal displacement and the surface virtual displacement at surface node $I_s,\ I_s = 1, 2, \ldots N_{node}$. Note that the surface FEM nodes are a subset of the bulk FEM nodes, and the virtual displacements of the surface nodes are not independent

with the virtual displacements of the bulk nodes. There is a connectivity map, say $Map_c(I_s)$, to connect the two, i.e. $Map_c(I_s) = I$ or vice versa.

Let

$$\mathbf{f}_L^{adh} := \int_{\Omega_S} \beta_L \beta_S \frac{\partial \phi(r)}{\partial \mathbf{x}_L} d v_S.$$

By substituting Eqs. (40)–(43) into Eq. (39), the preceding weak form becomes

$$\sum_{I=1}^{N_{node}} \sum_{J=1}^{N_{node}} \mathbf{w}_I \cdot \int_{\Omega_L} \rho N_I(\mathbf{x}) N_J(\mathbf{x}) \ddot{\mathbf{d}}_J(t) d v_L = -\sum_{I=1}^{N_{node}} \mathbf{w}_I \cdot \int_{\Omega_L} \boldsymbol{\sigma} \frac{\partial N_I}{\partial \mathbf{x}} d v_L + \sum_{I=1}^{N_{node}} \mathbf{w}_I \cdot \int_{\Omega_L} \rho N_I(\mathbf{x}) \mathbf{b} d v_L - \sum_{I=1}^{N_{node}} \mathbf{w}_I \cdot \int_{\Omega_L} N_I(\mathbf{x}) \mathbf{f}_L^{(adh)} d v_L + \sum_{I_s=1}^{N_{Snode}} \mathbf{w}_{I_s} \cdot \int_{\partial \Omega_L} N_{I_s}(\mathbf{x}) \mathbf{f}^{D,L} d s_L. \tag{44}$$

Due to the arbitrariness of the virtual displacements, e.g. $\forall \mathbf{w}_I \in H^1(\Omega)$, Eq. (44) can be cast into the following algebraic equations,

$$\mathbf{M} \ddot{\mathbf{d}}_L = \mathbf{F}_L^{ext} - \mathbf{F}_L^{int} + \mathbf{F}_L^{adh} + \mathbf{F}_L^{srf}, \tag{45}$$

where

$$\mathbf{M} = \sum_{I=1}^{N_{node}} \sum_{J=1}^{N_{node}} \int_{\Omega_L} \rho_L N_I(\mathbf{x}) N_J(\mathbf{x}) d v_L, \tag{46}$$

$$\mathbf{F}_L^{int} = \sum_{I=1}^{N_{node}} \int_{\Omega_L} \boldsymbol{\sigma} \frac{\partial N_I}{\partial \mathbf{x}} d v_L, \tag{47}$$

$$\mathbf{F}_L^{ext} = \sum_{I=1}^{N_{node}} \int_{\Omega_L} \rho_L N_I(\mathbf{x}) \mathbf{b} d v_L, \tag{48}$$

$$\mathbf{F}_L^{adh} = \sum_{I=1}^{N_{node}} \int_{\Omega_L} N_I(\mathbf{x}) \mathbf{f}_L^{(adh)} d v_L, \tag{49}$$

$$\mathbf{F}_L^{srf} = \sum_{I_s=1}^{N_{Snode}} \int_{\partial \Omega_L} N_{I_s}(\mathbf{x}) \mathbf{f}^{D,L} d s_L, \tag{50}$$

where N_{node} is the total number of FEM nodes in the liquid phase, whereas N_{Snode} is the total of FEM nodes on the liquid phase surface, which is a subset of the total bulk FEM nodes. The internal force for the surface node have all four sources of contribution. Eqs. (44) and (45) are the final discrete finite element dynamic equations for multiscale dynamic wetting model.

4.2. Surface tension force

In Eq. (44), the only new term is the last term, which is due to the contribution of surface tension or surface energy. We call $\mathbf{F}_L^{srf}$ as the surface tension force in liquid phase. Based on Eq. (38), this force can be re-written in two different forms,

$$\mathbf{F}_L^{srf} = \sum_{I_s=1}^{N_{Snode}} \left\{ \int_{\Gamma_{LS}} N_{I_s}(\mathbf{x}) \nabla_s \boldsymbol{\varsigma}_{LS} d s + \int_{\Gamma_{LG}} N_{I_s}(\mathbf{x}) \nabla_s \boldsymbol{\varsigma}_{LG} d s + \int_{\Gamma_{SG}} N_{I_s}(\mathbf{x}) \nabla_s \boldsymbol{\varsigma}_{SG} d s \right\}, \tag{51}$$

or

$$\mathbf{F}_L^{srf} = \sum_{I_s=1}^{N_{Snode}} \left\{ \left(N_{I_s}(x) \boldsymbol{\varsigma}_{LS}|_{x \in \partial \Gamma_{LS}} - \int_{\Gamma_{LS}} \frac{\partial N_{I_s}}{\partial \mathbf{x}} : \boldsymbol{\varsigma}_{LS} d s \right) + \left(N_{I_s}(x) \boldsymbol{\varsigma}_{LG}|_{x \in \partial \Gamma_{LG}} - \int_{\Gamma_{LG}} \frac{\partial N_{I_s}}{\partial \mathbf{x}} : \boldsymbol{\varsigma}_{LG} d s \right) + \left(N_{I_s}(x) \boldsymbol{\varsigma}_{SG}|_{x \in \partial \Gamma_{SG}} - \int_{\Gamma_{SG}} \frac{\partial N_{I_s}}{\partial \mathbf{x}} : \boldsymbol{\varsigma}_{SG} d s \right) \right\}. \tag{52}$$

The above two formulations, Eqs. (51) and (52), are equivalent in mathematics, because the second expression is just the integration by parts of the first expression. However, the two formulations lead two completely different implementation procedures in the finite element computation.

We first consider Eq. (51). As shown in Section 3, if we neglect the surface energy gradient and surface displacement gradient, we may write,

$$\nabla_s \boldsymbol{\varsigma}_{LS} = 2\gamma_{LS} \kappa \mathbf{n}, \quad \nabla_s \boldsymbol{\varsigma}_{LG} = 2\gamma_{LG} \kappa \mathbf{n}, \quad \text{and} \quad \nabla_s \boldsymbol{\varsigma}_{SG} = 2\gamma_{SG} \kappa \mathbf{n}. \tag{53}$$

where $\nabla_s = \nabla - \mathbf{n}(\mathbf{n} \cdot \nabla)$ is the surface gradient operator. Based on the above expressions, once we have found the value of the surface curvature and surface normal, we can compute the surface force due to surface tension, and the surface tension effect can be incorporated into the finite element simulation.

In passing, we note that it is a challenge to calculate the surface curvature at any point of an arbitrary surface in finite element computations. This is because that in finite element calculations, it is difficult to track surface evolution of a complex shaped continuum body and to calculate the surface curvature. However, in total Lagrangian finite element method, it is easy to track the trajectory of any material point. If we know the position of a surface material point at the current spatial configuration, we can use the Nanson formula to find the surface curvature.

Assume that surface normal vector in the reference configuration $\mathbf{N}$ is known, by Nanson's formula [31], we have

$$\mathbf{n}da = J\mathbf{F}^{-T}\mathbf{N}dA, \tag{54}$$

where da and dA are the infinitesimal areas in the current and reference configuration respectively, $\mathbf{F}$ is the deformation gradient tensor, and $J = \det \mathbf{F}$ is the determinant of the deformation gradient. Subsequently, the following relationship between the normal vector in the current and reference configuration may be obtained,

$$\mathbf{n} = \frac{\mathbf{F}^{-\mathbf{T}}\mathbf{N}}{\sqrt{\mathbf{N}\cdot\mathbf{C}^{-\mathbf{1}}\mathbf{N}}} \tag{55}$$

where $\mathbf{C}$ is the right Cauchy–Green tensor,

$$\mathbf{C} = \mathbf{F}^T\mathbf{F}. \tag{56}$$

The mean curvature is related to the divergence of the surface normal (e.g. [36]) as

$$2\kappa = -\nabla\cdot\mathbf{n}. \tag{57}$$

By substituting Eq. (55) into Eq. (57), the following equation can be obtained (see Appendix A for detailed derivation),

$$2\kappa = \frac{\mathbf{F}^T\mathcal{G}\vdots\left(\mathbf{C}^{-1}\mathbf{N}\otimes\mathbf{C}^{-1}\mathbf{N}\otimes\mathbf{C}^{-1}\mathbf{N}\right) - \nabla_{\mathbf{X}}\mathbf{N} : \left(\mathbf{C}^{-1}\mathbf{N}\otimes\mathbf{C}^{-1}\mathbf{N}\right)}{\left(\mathbf{N}\cdot\mathbf{C}^{-1}\mathbf{N}\right)^{3/2}} - \left(\mathbf{n}^T\mathcal{G}\right) : \mathbf{C}^{-1} + \sqrt{\mathbf{N}\cdot\mathbf{C}^{-1}\mathbf{N}}\mathbf{C}^{-1} : \nabla_{\mathbf{X}}\mathbf{N}, \tag{58}$$

where $\mathcal{G}$ is the derivative of the deformation gradient tensor, and it is defined as,

$$\mathcal{G} := \frac{\partial^2\mathbf{x}}{\partial\mathbf{X}\otimes\partial\mathbf{X}}. \tag{59}$$

One can see that using Eq. (51) to calculate the surface tension force requires the calculations of normal vector and the surface curvature in the current configuration. In order to compute these quantities, we have to first compute the deformation gradient and its derivatives. These calculations are computationally expensive. To improve the computational efficiency of MDWM, we have used Eq. (52) to develop a systematic procedure in calculating finite element nodal force due to surface tension, i.e.

$$\mathbf{F}_L^{srf} = -\sum_{I_s=1}^{N_{Snode}}\left\{\int_{\Gamma_{LS}}\frac{\partial N_{I_s}}{\partial\mathbf{x}}\cdot\varsigma_{LS}ds + \int_{\Gamma_{LG}}\frac{\partial N_{I_s}}{\partial\mathbf{x}}\cdot\varsigma_{LG}ds + \int_{\Gamma_{SG}}\frac{\partial N_{I_s}}{\partial\mathbf{x}}\cdot\varsigma_{SG}ds\right\}.$$

This formulation is very useful, when the surface elemental stress ς_{LS}, ς_{LG}, ς_{SG} are constant surface tensors. This is because, if the elemental surface stress is constant, we can choose linear finite element interpolation function for the surface element so that for a fixed surface element J,

$$\int_{S_J}\frac{\partial N_I}{\partial\mathbf{x}}ds = \pm\mathbf{I}_s^{S_J},$$

where $\mathbf{I}_s^{S_J}$ is the unit surface tensor of the surface patch S_J. Here both I and J are free indices.

Therefore, Eq. (52) suggests a very simple way to calculate surface tension force. The following is how it works:

First, the surface tension is defined as the force per unit length, where the force is within the surface, and it is perpendicular to surface element edge or boundary, e.g. [30], as shown in Fig. 6. Note that in Fig. 6 the direction of the surface tension is depicted as internal force.

If the thickness of the surface element is in unit length, in 2D cases the surface tension with unit (N/m) is simply the surface force (N). Thus we may apply the surface tension as the surface force to each node of the surface patch, and the direction of the force is parallel to the edge of the surface patch, shown in Fig. 7. By taking the summation of the surface tension forces at each node, we can obtain the resultant forces. When two forces on a flat surface act in the opposite directions, the resultant force is zero on a flat surface as shown in Fig. 8. It is consistent with the surface traction theory, and the proposed surface tension model only requires to calculate the tangential direction of the surface patch and take the summation of the surface tension forces in two dimensional case. When two nodes of the surface patch are $\mathbf{x}_1$ and $\mathbf{x}_2$, the direction of the surface tension force at node $\mathbf{x}_1$ and $\mathbf{x}_2$ are given by $(\mathbf{x}_2-\mathbf{x}_1)/\mid\mathbf{x}_2-\mathbf{x}_1\mid$ and $(\mathbf{x}_1-\mathbf{x}_2)/\mid\mathbf{x}_2-\mathbf{x}_1\mid$. For example, in the case shown in Fig. 8, the surface tension forces at node 1 and 2 are given by

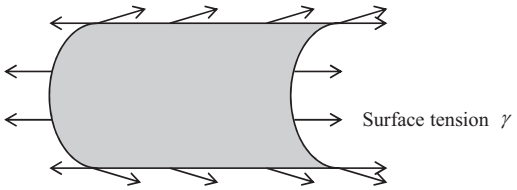

Fig. 6. Surface tension acts on a surface patch in three dimensional space.

$$\mathbf{F}_{L,1}^{srf} = \gamma \frac{\mathbf{x}_2 - \mathbf{x}_1}{|\,\mathbf{x}_2 - \mathbf{x}_1\,|} + \gamma \frac{\mathbf{x}_5 - \mathbf{x}_1}{|\,\mathbf{x}_5 - \mathbf{x}_1\,|} = \gamma \begin{pmatrix} 1 \\ 0 \end{pmatrix} + \gamma \begin{pmatrix} 0 \\ 1 \end{pmatrix} = \gamma \begin{pmatrix} 1 \\ 1 \end{pmatrix}, \tag{60}$$

and

$$\mathbf{F}_{L,2}^{srf} = \gamma \frac{\mathbf{x}_1 - \mathbf{x}_2}{|\,\mathbf{x}_2 - \mathbf{x}_1\,|} + \gamma \frac{\mathbf{x}_3 - \mathbf{x}_2}{|\,\mathbf{x}_3 - \mathbf{x}_2\,|} = \gamma \begin{pmatrix} -1 \\ 0 \end{pmatrix} + \gamma \begin{pmatrix} 1 \\ 0 \end{pmatrix} = \begin{pmatrix} 0 \\ 0 \end{pmatrix}. \tag{61}$$

In the three dimensional case, it is necessary to multiply the half of the edge length, since the unit of the surface tension is the force per unit length (N/m), and there are two nodes in each edge for linear elements. The direction of the surface tension force can be obtained by following way: First, we compute normal vector of the patch at node $\mathbf{x}_1$ by cross product as shown in Fig. 9,

$$\mathbf{n} = \frac{(\mathbf{x}_2 - \mathbf{x}_1)}{|\,\mathbf{x}_2 - \mathbf{x}_1\,|} \times \frac{(\mathbf{x}_4 - \mathbf{x}_1)}{|\,\mathbf{x}_4 - \mathbf{x}_1\,|}. \tag{62}$$

Eq. (62) can be replaced by Eq. (55) when the normal vector in the reference configuration is known. Note that the inner product of the direction of the surface tension force $\mathbf{e}$ and vector $\mathbf{x}_2 - \mathbf{x}_1$ is zero, because that the surface tension is perpendicular to the line. In addition, the cross product of $(\mathbf{x}_2 - \mathbf{x}_1)/|\,\mathbf{x}_2 - \mathbf{x}_1\,|$ and $\mathbf{e}$ equals $\mathbf{n}$ because the surface tension is parallel to the surface. Thus the direction of the surface tension force $\mathbf{e}$ can be obtained by computing the cross product of $\mathbf{n}$ and $(\mathbf{x}_2 - \mathbf{x}_1)/|\,\mathbf{x}_2 - \mathbf{x}_1\,|$,

$$\mathbf{e} = \mathbf{n} \times \frac{(\mathbf{x}_2 - \mathbf{x}_1)}{|\,\mathbf{x}_2 - \mathbf{x}_1\,|}. \tag{63}$$

When there is no torsion in the surface patch, the direction of the surface tension at each node in an edge are the same. However, since there may exist torsion after the deformation, we should compute the direction of the surface tension at each node in an edge checking for the consistency with the neighbor surface patch. Finally, in three dimensional case, the proposed element surface tension model needs to calculate normal vector of the surface patch at each node and the direction of surface tension and the length of the element edge.

5. Moving contact line formulation I: constant surface stress

The heart of the multiscale dynamic wetting model is multiscale moving contact line formulation, which is a finite element formulation for surface tension force at the intersection of the gas/liquid/solid interface. Because the contact line is the place where three phases in juncture, the differences of three surface energy at the contact line will drive the droplet spreading. In this Section, we discuss the technical procedure of the multiscale contact line formulation, and it is essentially a modified dynamic Young–Laplace equation [50] in the framework of multiscale dynamic wetting theory with finite element formulation.

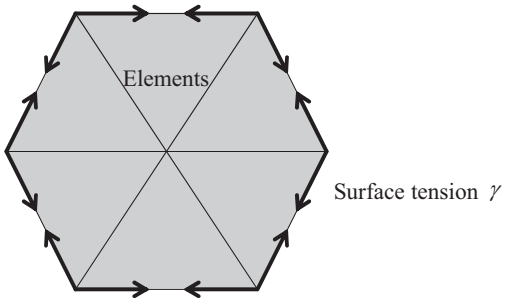

Fig. 7. The proposed surface tension model in two dimensional case.

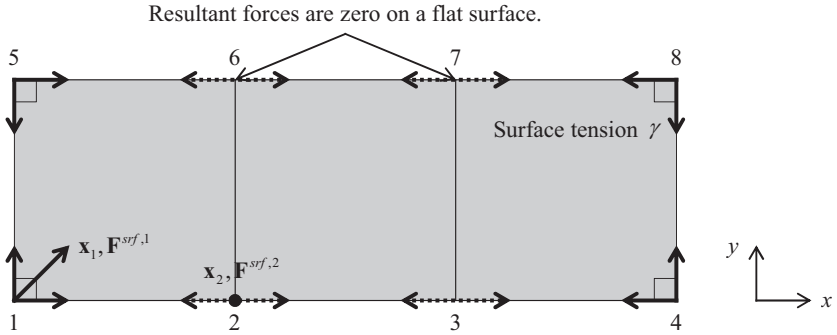

Fig. 8. The resultant surface tension force on a flat surface.

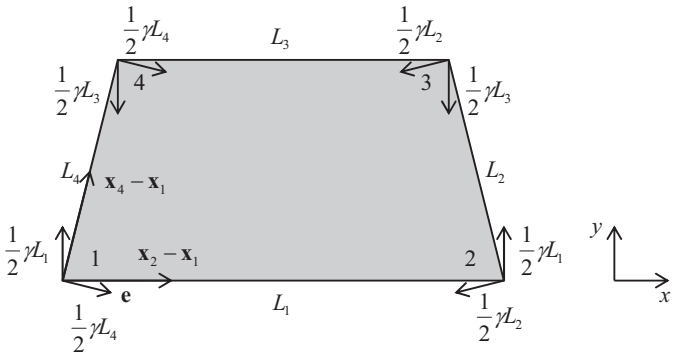

Fig. 9. The direction of the surface tension force at surface nodes.

The proposed moving contact line formulation is mainly based on Eq. (52). We shall discuss the contact line formulation for two different cases: (I) the special case with constant surface stress only, and (II) the general case with non-uniform surface stress state. In this section, we shall discuss the case (I) first.

First, we consider a special case of constant surface stress, i.e.

$$\varsigma_{LS} = \gamma_{LS}\mathbf{I}_s^{(LS)}, \quad \varsigma_{LG} = \gamma_{LG}\mathbf{I}_s^{(LG)}, \quad \text{and} \quad \varsigma_{SG} = \gamma_{SG}\mathbf{I}_s^{(SG)},$$

where $\mathbf{I}_s^{(LS)}$, $\mathbf{I}_s^{(LG)}$, and $\mathbf{I}_s^{(SG)}$ are the unit tensors on LS, LG, and SG interface. In this case, the internal force due the surface stress contribution at the edge node I on the contact line can be obtained as,

$$\mathbf{F}_{L,I}^{srf} = -\left(\int_{\Gamma_{LS}} \frac{\partial N_I}{\partial \mathbf{x}} \cdot \gamma_{LS}\mathbf{I}_s^{(LS)} ds + \int_{\Gamma_{LG}} \frac{\partial N_I}{\partial \mathbf{x}} \cdot \gamma_{LG}\mathbf{I}_s^{(LG)} ds + \int_{\Gamma_{SG}} \frac{\partial N_I}{\partial \mathbf{x}} \cdot \gamma_{SG}\mathbf{I}_s^{(SG)} ds\right). \tag{64}$$

Fig. 10 illustrates surface patches at the contact line in a setting of two-dimensional finite element computations. The edge node in Fig. 10 is the contact line node. Surrounding that node, one may find that for linear FEM shape function,

$$\int_{\Gamma_{LG}} \frac{\partial N_I}{\partial \mathbf{x}} ds = \begin{pmatrix} \cos\theta \\ -\sin\theta \end{pmatrix}, \quad \int_{\Gamma_{LS}} \frac{\partial N_I}{\partial \mathbf{x}} ds = \begin{pmatrix} 1 \\ 0 \end{pmatrix}, \quad \text{and} \quad \int_{\Gamma_{SG}} \frac{\partial N_I}{\partial \mathbf{x}} ds = -\begin{pmatrix} 1 \\ 0 \end{pmatrix}. \tag{65}$$

Substituting Eq. (65) into (64) and projecting the surface tension force to the global coordinate system that is formed by the tangential and normal vectors of the solid surface as shown in Fig. 10, we have the surface tension force at the contact line node I as

$$\mathbf{F}_{L,I}^{srf} = \boldsymbol{\gamma}_{LG} + \boldsymbol{\gamma}_{LS} + \boldsymbol{\gamma}_{SG},$$

where

$$\boldsymbol{\gamma}_{LG} = \begin{pmatrix} -\gamma_{LG}\cos\theta \\ \gamma_{LG}\sin\theta \end{pmatrix}, \quad \boldsymbol{\gamma}_{LS} = \begin{pmatrix} -\gamma_{LS} \\ 0 \end{pmatrix} \tag{66}$$

and

$$\boldsymbol{\gamma}_{SG} = \begin{pmatrix} \gamma_{SG} \\ 0 \end{pmatrix}. \tag{67}$$

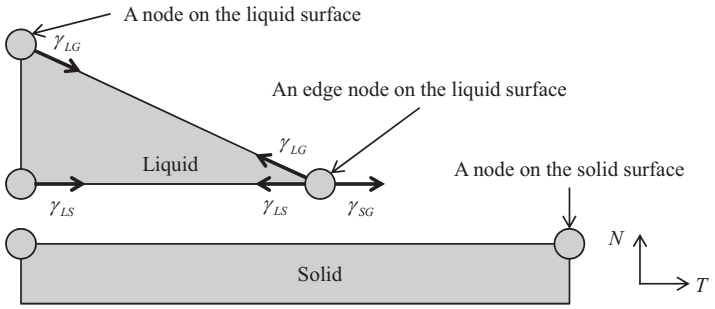

Fig. 10. Surface patches at the contact line in two dimensional space.

Note that the angle θ in (66) is the actual (dynamic) contact angle, and we measure it based on the position and orientation of the liquid element at the contact line at each time step. The particular θ used at the time step n for $\mathbf{F}_{L,I}^{srf}(n\Delta t)$ is dynamic contact angle calculated at the time step n-1, i.e. θ_{n-1}.

Finally, the resultant force of the node at the contact line $\mathbf{F}_{L,I}^{srf}$ is given by

$$\mathbf{F}_{L,I}^{srf} = \boldsymbol{\gamma}_{SG} + \boldsymbol{\gamma}_{LG} + \boldsymbol{\gamma}_{LS} \tag{68}$$

$$= \begin{pmatrix} \gamma_{SG} - \gamma_{LG}\cos\theta - \gamma_{LS} \\ \gamma_{LG}\sin\theta \end{pmatrix}. \tag{69}$$

5.1. Implementation in 2D finite element analysis

In the case of two dimensional Finite Element Method, the linear surface patch degenerates to two finite element nodes. Fig. 11 shows three different cases of the surface patch of the liquid in the two dimensional Finite Element implementation of MDWM.

- Case a (Fig. 11(a)):
  Neither of two nodes are in contact with the solid surface.
  The surface energy between the liquid and gas γ_{LG} is applied to the surface patch, because the surface patch is fully in contact with the gas;
- Case b (Fig. 11(b)):
  One of the nodes is in contact with the solid surface.
  The surface energy between the liquid and gas γ_{LG} is applied to the surface patch. In addition, the surface energy between the solid and gas γ_{SG} is applied to the node which is in contact with the solid surface in the tangential direction of the solid surface;
- Case c (Fig. 11(c)):
  Both of the nodes are in contact with the solid surface.
  The surface energy between the liquid and solid γ_{LS} is applied to the surface patch, because this surface patch is fully in contact with the solid surface.

5.2. Surface element in 3D FEM discretization

Fig. 12 shows the triangular surface patches in a three-dimensional finite element surface mesh. For a triangular surface patch, we need to distinguish the following four cases:

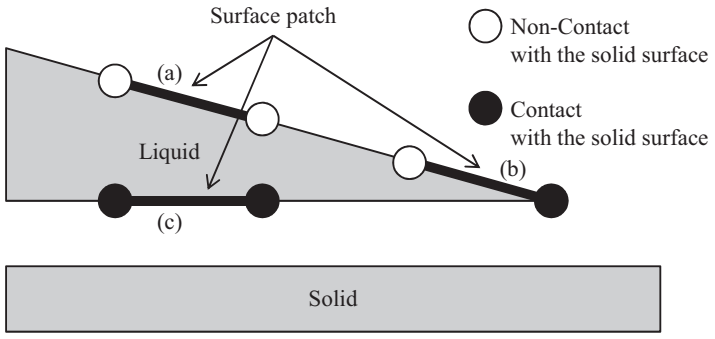

Fig. 11. Three cases of the liquid surface patch in 2D finite element discretization.

- Case a (Fig. 12(a)):
  None of the three nodes are in contact with the solid surface.
  The surface energy between the liquid and gas phases, γ_{LG}, is applied to all edges a, b and $c$based on the proposed FEM surface tension model, because the surface patch is fully in contact with the gas;
- Case b (Fig. 12(b)):
  Only one of the nodes is in contact with the solid surface.
  The surface energy between the liquid and gas phases, γ_{LG}, is applied to the all edges, the same as Case a;
- Case c (Fig. 13(c)):
  Two nodes are in contact with the solid surface.
  The surface energy between the liquid and gas phases, γ_{LG}, is applied to all edges. Additionally the surface energy between the solid and gas phases, γ_{SG}, is applied to the edge a. The direction of the surface tension γ_{SG} is shown in Fig. 13, where $\mathbf{n}$ is the normal vector of the solid surface, and $\mathbf{x}_a$ is the unit vector of the edge a, and $\mathbf{e}$ is the direction of γ_{SG}. The direction of the surface tension between the solid and gas phases, $\mathbf{e}$, can be obtained by the cross product,

$$\mathbf{e} = \mathbf{x}_a \times \mathbf{n}. \tag{70}$$

- Case d (Fig. 12(d)):
  All nodes are in contact with the solid surface.
  The surface energy between the liquid and solid phases, γ_{LS}, is applied to all edges, because the surface patch is fully in contact with the solid surface.

Fig. 14 shows all possible cases of the rectangular surface patches in 3D finite element mesh surface. For rectangular surface patches, there are five cases.

- Case a (Fig. 14(a)):
  None of the nodes are in contact with the solid surface.
  The surface energy between the liquid and gas phases, γ_{LG}, is applied to the all edges a, b, c and d based on the proposed FEM surface tension model, because the surface patch is fully in contact with the gas;
- Case b (Fig. 14(b)):
  Only one of the nodes is in contact with the solid surface.
  The surface energy between the liquid and gas phases, γ_{LG}, is applied to all edges, the same as Case a.
- Case c (Fig. 14(c)):
  Two nodes are contact with the solid surface.
  The surface energy between the liquid and gas phases, γ_{LG}, is applied to all edges. Subsequently, the surface tension between the solid and gas phase, γ_{SG} ,is applied to the edge a. The direction of γ_{SG} can be obtained by Eq. (70);
- Case d (Fig. 14(d)):
  Three nodes are in contact with the solid surface.
  The surface energy between the liquid and gas phases, γ_{LG}, is applied to all edges. Moreover, the surface energy between the solid and gas phases, γ_{SG}, is applied to the edge $a$and b. The direction of γ_{SG} can then be obtained by Eq. (70).
- Case e (Fig. 14(e)):
  All nodes are in contact with the solid surface.
  The surface energy between the liquid and solid phases, γ_{LS}, is applied to all edges, because the surface patch is fully in contact with the solid surface.

6. Moving contact line formulation II: general surface stress state

One of the main advantages of the above multiscale moving contact-line formulation is that it does not require quadrature integration on the moving surface elements. However, when the surface stress is generally not constant in the surface

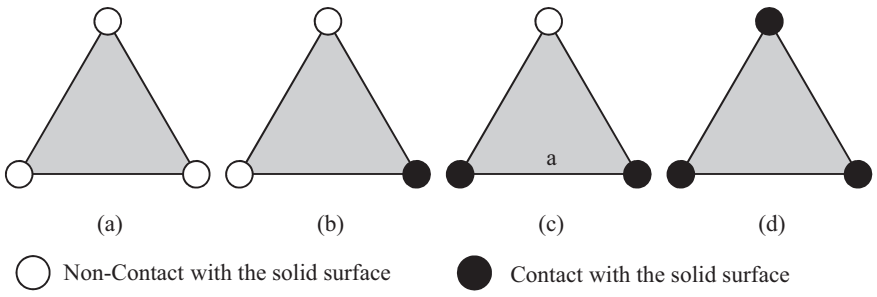

Fig. 12. The triangular surface patches of the liquid in the three-dimensional finite element implementation.

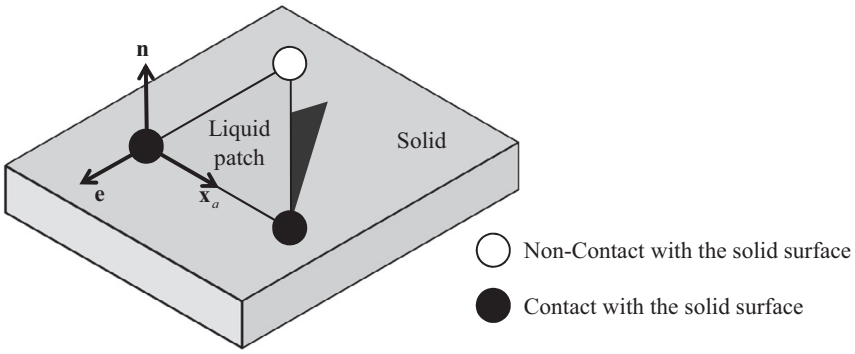

Fig. 13. The direction of the surface tension between the solid and gas phases.

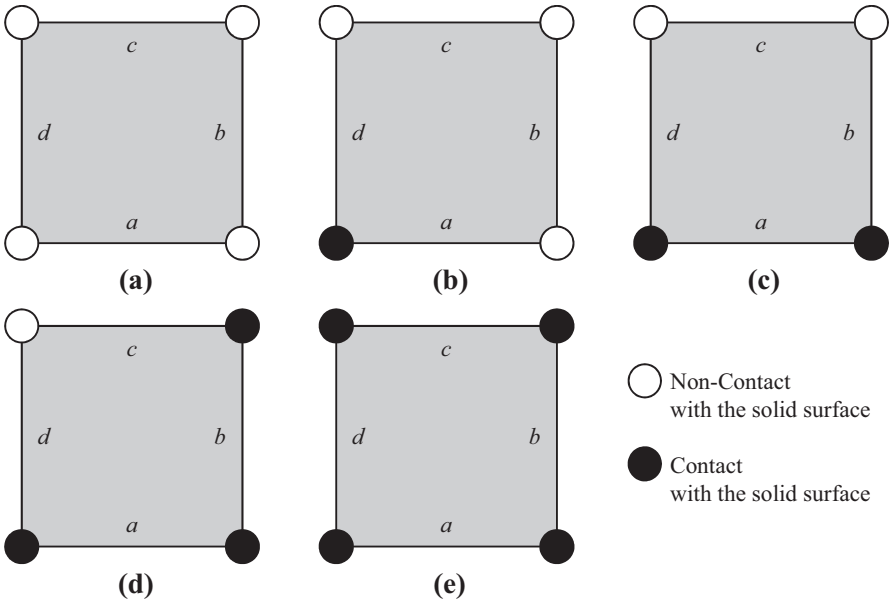

Fig. 14. Rectangular surface patches on the droplet surface in 3D finite element analysis.

element, the simple procedure discussed in previous section is not applicable anymore. According to Eq. (13), on the general solid phase surface, we have

$$\varsigma_S = \gamma_S \mathbf{I}_s^{(S)} + \frac{\partial \Gamma_S}{\partial \boldsymbol{\epsilon}_s} + \gamma_S \nabla_s \otimes \mathbf{u}$$

and on the surface of a viscous fluid phase (Eq. (12)), we have

$$\varsigma_L = \gamma_L \mathbf{I}_s^{(L)} + \nabla_s \gamma_L.$$

Suppose that the liquid–solid interphase is compatible. The most complex surface stress constitute model on liquid–solid interface may be,

$$\varsigma_{LS} = \gamma_{LS} \mathbf{I}_s^{(LS)} + \nabla_s \gamma_L + \frac{\partial \Gamma_S}{\partial \boldsymbol{\epsilon}_s} + \gamma_S \nabla_s \otimes \mathbf{u}.$$

Similar situations occur in the gas–solid interface as well as the gas–liquid interface, if complex fluid models are involved.

Hence, the surface stress may vary within a surface element for general triple phase systems. Considering general cases with inhomogeneous surface stress distribution, we cannot apply the procedure illustrated in Section 5 to obtain the nodal surface force without integrating surface weak formulation in a surface element. The surface force due to inhomogeneous surface stress field has to be calculated based the surface Galerkin weak form and surface element discretization, i.e.

$$\mathbf{F}_{L,I}^{srf} = -\int_{\Gamma_{SG}} \varsigma_{SG} \frac{\partial N_I}{\partial \mathbf{x}} ds - \int_{\Gamma_{LS}} \varsigma_{LS} \frac{\partial N_I}{\partial \mathbf{x}} ds - \int_{\Gamma_{LG}} \varsigma_{LG} \frac{\partial N_I}{\partial \mathbf{x}} ds, \tag{71}$$

in which the surface stress may be non-uniform.

To do so, we must first make sure that we have compatible finite element meshes on the both sides of an interphase. Taking the liquid–solid interphase as an example, we must have compatible meshes on both liquid surface and solid surface such that the FEM nodal force transfer is consistent across the interphase. To have a compatible finite element mesh on the both side of an interface, we introduce the following virtual solid surface approach.

6.1. Virtual solid surface

In the derivation of the surface weak form, we have implicitly assumed that at the element level the surface area of the eth elements on two different surfaces have the relation: $\Gamma_{SL}(e) = \Gamma_{LS}(e)$. However, in MDWM finite element implementation, the positions of the liquid and solid nodes are generally different along the interface, because there is a relative movement between the liquid FEM nodes and solid FEM nodes. Therefore at the element level, $I_s(SL) \neq I_s(LS),\ I_s = 1, 2 \ldots N_{Snode}$.

To solve this dilemma, a virtual solid surface is introduced. To illustrate the concept, we first illustrate the virtual surface approach in the two dimensional case as shown in Fig. 15. In Fig. 15, the positions of solid nodes on the virtual solid surface are exactly the same as the positions of liquid nodes on the moving liquid surface. The values of any physical variable at the virtual nodes on the solid surface are obtained from that of the fixed solid nodes on the real solid surface by using the isoparametric interpolation [1,21],

$$f(\mathbf{x}) = \sum_{I=1}^{nnode} N_I(\xi) f_I, \tag{72}$$

where f is a general field variable, which can be a scalar or vector field; *nnode* is the number of nodes in an element, $N_I(\xi)$ is the FEM shape function for node I, and f_I is the nodal value of the field variable at the fixed node I, and *nnode* is the total number of nodes in an element. Note that since index I is a dummy index, we do not need to specific it as I_s without confusion.

This can be done provided that we know the parametric coordinate of the virtual node ξ and which element it belongs to. In computations, we always know the position of a liquid surface node, which is exactly the position of the corresponding virtual solid node.

The natural coordinate ξ and the physical coordinate $\mathbf{x}$ are related by the mapping

$$\mathbf{x} = \Phi(\xi).$$

For 2D cases, the surface patch is a one dimensional element; and in 3D cases, the surface patch is a two dimensional element. Fig. 16 shows how to locate a virtual node in a fixed element. By using Eq. (72), the natural coordinate can be obtained by inverting the following equations,

$$\mathbf{0} = \sum_{I=1}^{nnode} N_I(\xi)\mathbf{x}_I - \mathbf{x}, \tag{73}$$

where *nnode* is the number of nodes in an element.

In the case of 1D linear elements, Eq. (73) becomes a linear equation, and it can be solved directly as follows,

$$0 = N_1(\xi)x_1 + N_2(\xi)x_2, \tag{74}$$

$$\xi = 2\frac{x - x_1}{x_2 - x_1} - 1. \tag{75}$$

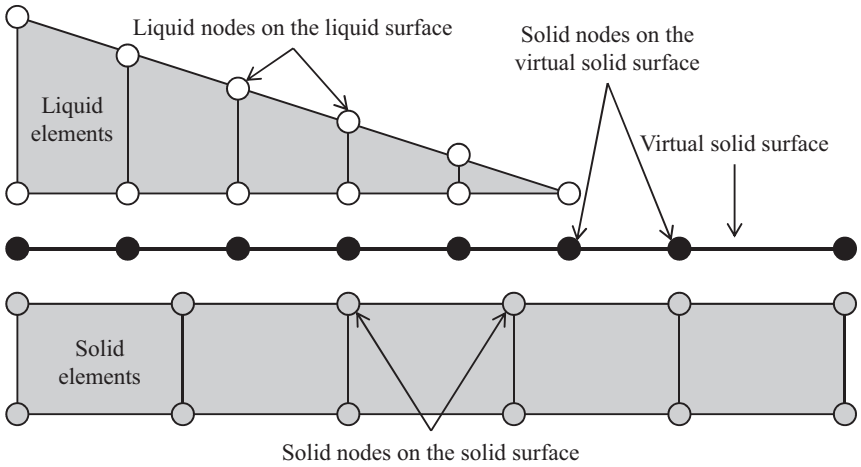

Fig. 15. A virtual solid surface in two dimensional case.

In general, Eq. (73) cannot be solved directly for higher order elements, for instance, the two dimensional quadrilateral element, this is because that it is a non-linear algebraic equation due to the bilinear term. The standard Newton–Raphson method may be used to numerically invert Eq. (73), and the following is a step-by-step solution procedure,

$$\mathbf{F}(\xi) = \sum_{I=1}^{nnode} N_I(\xi)\mathbf{x}_I - \mathbf{x} = \mathbf{0}, \tag{76}$$

$$\mathbf{F}\left(\xi^i\right) \approx \mathbf{F}\left(\xi^{i-1}\right) + \mathbf{F}'\left(\xi^{i-1}\right)\left(\xi^i - \xi^{i-1}\right), \tag{77}$$

$$\xi^i \approx \xi^{i-1} - \mathbf{F}\prime^{-1}\left(\xi^{i-1}\right)\mathbf{F}\left(\xi^i\right), \tag{78}$$

where ξ^i is the ith iterative solution, and $i = 1, 2, \ldots, N$ denoting the iteration of the Newton–Raphson method. In Eq. (78),

$$\mathbf{F}'(\xi) = \sum_{I=1}^{nnode} \frac{\partial N_I}{\partial \xi}(\xi)\mathbf{x}_I. \tag{79}$$

Since the Newton–Raphson method has quadratic convergence rate, it only takes a few steps to find the numerical solution of Eq. (76).

6.2. Two dimensional finite element analysis for dynamical wetting

In the following, we discuss how to implement Eq. (71) in two dimensional finite element computations. Here the surface patch is a one dimensional surface element as shown in Fig. 17. In Fig. 17, $\mathbf{x}$ denotes global coordinate, $\mathbf{x}'$ denotes local coordinate that x' axis and y' axis are parallel and perpendicular to the surface patch, and θ is the angle between $x$and x' axis. Then, the relationship between $\mathbf{x}$-axis and $\mathbf{x}'$-axis is given as

$$\mathbf{x}' = \mathbf{R}\mathbf{x}, \tag{80}$$

where

$$\mathbf{R}^T = \begin{pmatrix} \cos\theta & -\sin\theta \\ \sin\theta & \cos\theta \end{pmatrix} = \frac{1}{L}\begin{pmatrix} x_2 - x_1 & y_1 - y_2 \\ y_2 - y_1 & x_2 - x_1 \end{pmatrix}, \tag{81}$$

where $L = |\ \mathbf{x}_2 - \mathbf{x}_1\ |$ is the length of the surface patch. The local coordinates of the node I are given by

$$\mathbf{x}'_I = \mathbf{R}\mathbf{x}_I, \tag{82}$$

where $I = 1, 2$. Here, one dimensional Finite Element interpolation is used to compute the derivatives of FEM shape functions with respect to $\mathbf{x}'$,

$$\left[\frac{\partial N_I}{\partial \mathbf{x}'}\right]^T = \begin{bmatrix} \frac{\partial N_I}{\partial x'} & 0 \end{bmatrix}, \tag{83}$$

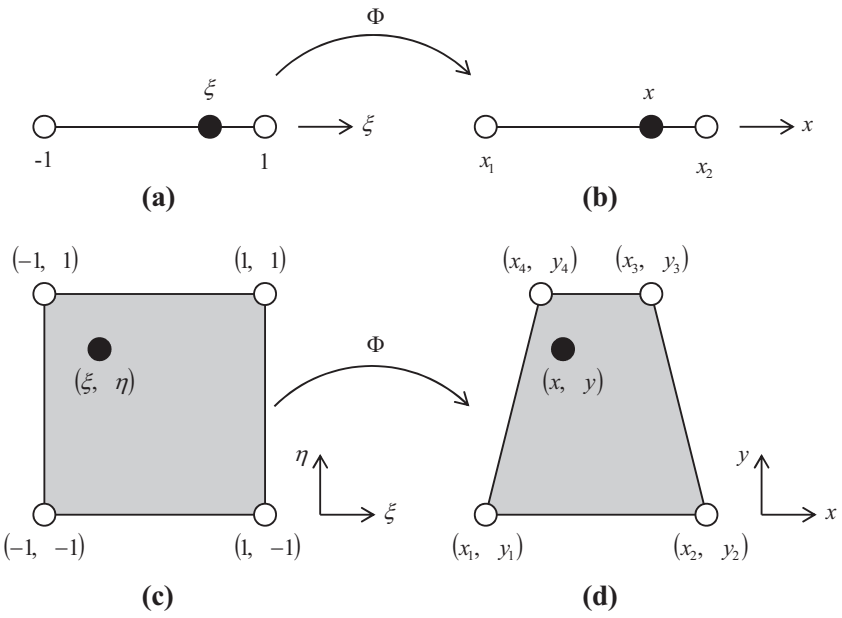

Fig. 16. The isoparametric interpolation.

where y' components of $\mathbf{x}'_1$ and $\mathbf{x}'_2$ are zero. The derivatives of shape function with respect to $\mathbf{x}$ is as follows,

$$\left[\frac{\partial N_I}{\partial \mathbf{x}}\right]^T = \left[\frac{\partial N_I}{\partial x} \quad \frac{\partial N_I}{\partial y}\right],$$

which can be obtained by using the chain rule,

$$\frac{\partial N_I}{\partial \mathbf{x}}^T = \frac{\partial N_I}{\partial \mathbf{x}'}^T \frac{\partial \mathbf{x}'}{\partial \mathbf{x}}. \tag{84}$$

From Eq. (80), we have

$$\frac{\partial \mathbf{x}'}{\partial \mathbf{x}} = \mathbf{R}. \tag{85}$$

Thus,

$$\frac{\partial N_I}{\partial \mathbf{x}}^T = \frac{\partial N_I}{\partial \mathbf{x}\prime}^T \mathbf{R} \quad \text{or} \quad \frac{\partial N_I}{\partial \mathbf{x}} = \mathbf{R}^T \frac{\partial N_I}{\partial \mathbf{x}'}. \tag{86}$$

Once the surface stress is obtained, the Γ_{LG} and Γ_{LS} terms in Eq. (38) can then be computed.

For the integration term over Γ^{SG} in Eq. (38), the solid–gas interface element is introduced. Fig. 18 shows the solid–gas interface element in the two dimensional FEM example. One can see that we only need the surface nodal force at node 1 in Fig. 18, and a shape function at node 1 is given by

$$N_1(x') = \frac{1}{L}(L - x'), \tag{87}$$

where L is the length of the solid–gas interface element, and x' is the local coordinate, $x' = 0$ at node 1 and $x' = L$ at node 2. The derivative of shape function with respect to $\mathbf{x}'$ is given by

$$\frac{\partial N_1}{\partial \mathbf{x}'} = \frac{1}{L}\begin{pmatrix} -1 \\ 0 \end{pmatrix}. \tag{88}$$

Thus the term Γ^{SG} in Eq. (38) can be written as,

$$\int_{\Gamma_{SG}} \varsigma_{SG} \frac{\partial N_I}{\partial \mathbf{x}} ds = \int_{\Gamma_{SG}} \varsigma^{SG} \mathbf{R}^T \frac{1}{L}\begin{pmatrix} -1 \\ 0 \end{pmatrix} ds \approx \frac{1}{2}\{\varsigma_{SG}(\mathbf{x}_1) + \varsigma_{SG}(\mathbf{x}_2)\}\mathbf{R}^T \begin{pmatrix} -1 \\ 0 \end{pmatrix}, \tag{89}$$

where the trapezoidal rule is used for the surface integration. In the case that $L \approx 0$ $\varsigma_{SG}(\mathbf{x}_1) \approx \varsigma_{SG}(\mathbf{x}_2)$. Finally, Γ_{SG} term in Eq. (38) is obtained as

$$\int_{\Gamma_{SG}} \varsigma_{SG} \frac{\partial N_1}{\partial \mathbf{x}} ds \approx \varsigma_{SG}(\mathbf{x}_1)\mathbf{R}^T \begin{pmatrix} -1 \\ 0 \end{pmatrix} \approx \varsigma_{SG}(\mathbf{x}_1) \begin{pmatrix} -\cos\theta \\ \sin\theta \end{pmatrix}. \tag{90}$$

6.3. 3D FEM formulation for dynamical wetting

For three-dimensional droplet spreading problems, the surface patch is a two dimensional element as shown in Fig. 19. In Fig. 19, $\mathbf{x}$ denotes the global coordinate, and $\mathbf{x}'$ denotes the local coordinate on the tangent space. The local coordinate is chosen such that x' is along the direction of the unit vector $\mathbf{x}_{21} = (\mathbf{x}_2 - \mathbf{x}_1)/\mid \mathbf{x}_2 - \mathbf{x}_1 \mid$, and the surface patch is in the x' -y' plane, and z'-axis is in the direction of the normal vector of the surface patch $\mathbf{n}$. The unit vector of y' axis, $\mathbf{y}_1$, is obtained by

$$\mathbf{y}_1 = \frac{\mathbf{n} \times \mathbf{x}_{21}}{\mid \mathbf{n} \times \mathbf{x}_{21} \mid}. \tag{91}$$

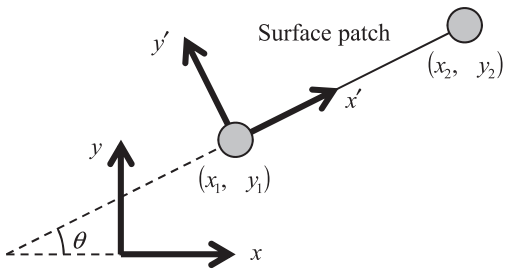

Fig. 17. Surface patch in 2D finite element analysis.

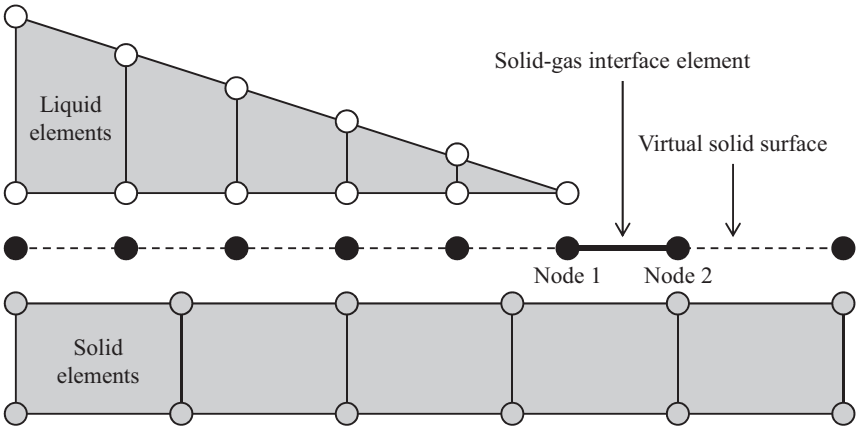

Fig. 18. Two-dimensional solid–gas interface element.

Then, the relationship between $\mathbf{x}$ and $\mathbf{x}'$ coordinate systems is given by

$$\mathbf{x}' = \mathbf{R}\mathbf{x}, \tag{92}$$

where

$$\mathbf{R}^T = (\mathbf{x}_{21}, \mathbf{y}_1, \mathbf{n}). \tag{93}$$

The local coordinates of node I, $I = 1,2,3,4$, is given by

$$\mathbf{x}'_I = \mathbf{R}\mathbf{x}_I. \tag{94}$$

Two dimensional finite element shape function can be used in the surface element, and we can then compute the derivatives of shape functions with respect to the local coordinate $\mathbf{x}'$,

$$\left[\frac{\partial N_I}{\partial \mathbf{x}'}\right]^T = \left[\frac{\partial N_I}{\partial x'} \quad \frac{\partial N_I}{\partial y'} \quad 0\right].$$

Since z' components of $\mathbf{x}'_I$ is zero. The derivatives of shape function with respect to $\mathbf{x}$ are,

$$\left[\frac{\partial N_I}{\partial \mathbf{x}}\right]^T = \left[\frac{\partial N_I}{\partial x} \quad \frac{\partial N_I}{\partial y} \quad \frac{\partial N_I}{\partial z}\right],$$

which can be obtained by using the chain rule, the same as the implementation in 2D case.

The solid–gas interface element in three-dimensional finite element calculation is shown in Fig. 20. In Fig. 20, L_1 is the length between node 1 and node 2, L_2 is the length between node 2 and node 3, and the shape of the solid–gas interface element is rectangular. We only need the nodal forces at node 1 and 2 in Fig. 20. The shape function at node 1 is given as

$$N_1(x', y') = \frac{1}{L_1 L_2}(L_1 - x')(L_2 - y'). \tag{95}$$

The derivative of shape function with respect to $\mathbf{x}'$ is given by

$$\frac{\partial N_1}{\partial \mathbf{x}'}(x', y') = \frac{1}{L_1 L_2}\begin{pmatrix} -(L_2 - y') \\ -(L_1 - x') \\ 0 \end{pmatrix}. \tag{96}$$

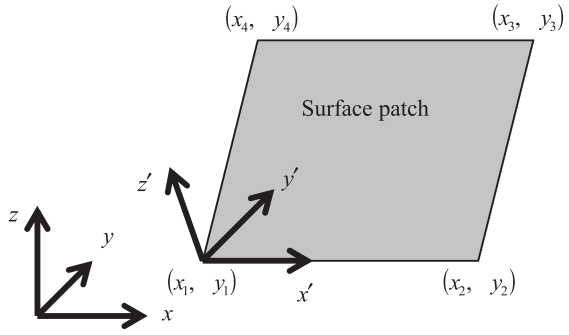

Fig. 19. Surface patch in the three dimensional FEM discretization.

Thus the surface weak form term on Γ_{SG} in Eq. (71) can be written as

$$\int_{\Gamma_{SG}} \varsigma_{SG} \frac{\partial N_1}{\partial \mathbf{x}} ds = \int_{\Gamma_{SG}} \varsigma_{SG} \mathbf{R}^T \frac{\partial N_1}{\partial \mathbf{x}'}(x', y') ds \approx \frac{L_1 L_2}{4} \left\{ \varsigma_{SG}(\mathbf{x}_1) \mathbf{R}^T \frac{\partial N_1}{\partial \mathbf{x}'}(0,0) + \varsigma_{SG}(\mathbf{x}_2) \mathbf{R}^T \frac{\partial N_1}{\partial \mathbf{x}'}(L_1, 0) \varsigma_{SG}(\mathbf{x}_3) \mathbf{R}^T \frac{\partial N_1}{\partial \mathbf{x}'}(L_1, L_2) + \varsigma_{SG}(\mathbf{x}_4) \mathbf{R}^T \frac{\partial N_1}{\partial \mathbf{x}'}(0, L_2) \right\} \approx -\frac{1}{4} \left\{ \varsigma_{SG}(\mathbf{x}_1) \mathbf{R}^T \begin{pmatrix} L_2 \\ L_1 \\ 0 \end{pmatrix} + \varsigma_{SG}(\mathbf{x}_2) \mathbf{R}^T \begin{pmatrix} L_2 \\ 0 \\ 0 \end{pmatrix} + \varsigma_{SG}(\mathbf{x}_4) \mathbf{R}^T \begin{pmatrix} 0 \\ L_1 \\ 0 \end{pmatrix} \right\}, \tag{97}$$

where the trapezoidal rule is applied to the surface quadrature integration. In the case that $L_2 \approx 0$, $\varsigma_{SG}(\mathbf{x}_1) \approx \varsigma_{SG}(\mathbf{x}_4)$. Finally, the integral term on Γ_{SG} in Eq. (38) at node 1 is obtained as

$$\int_{\Gamma_{SG}} \varsigma_{SG} \frac{\partial N_1}{\partial \mathbf{x}} ds \approx -\frac{L_1}{2} \varsigma_{SG}(\mathbf{x}_1) \mathbf{R}^T \begin{pmatrix} 0 \\ 1 \\ 0 \end{pmatrix} = -\frac{L_1}{2} \varsigma_{SG}(\mathbf{x}_1) \begin{pmatrix} y_{1x} \\ y_{1y} \\ y_{1z} \end{pmatrix}. \tag{98}$$

Similarly, the integration term on Γ_{SG} in Eq. (38) at the node 2 is given as

$$\int_{\Gamma_{SG}} \varsigma_{SG} \frac{\partial N_2}{\partial \mathbf{x}} ds \approx -\frac{L_1}{2} \varsigma_{SG}(\mathbf{x}_2) \mathbf{R}^T \begin{pmatrix} 0 \\ 1 \\ 0 \end{pmatrix} = -\frac{L_1}{2} \varsigma_{SG}(\mathbf{x}_2) \begin{pmatrix} y_{1x} \\ y_{1y} \\ y_{1z} \end{pmatrix}. \tag{99}$$

7. Numerical examples

7.1. Validation of the discrete surface tension model

In this section, we validate the proposed surface tension model by conducting a few numerical examples. In the first example, we exam the surface tension effect on two dimensional model of water drop as shown in Fig. 21. The initial shape of the water drop is an ellipse, and its major axis is 100 (nm) and its minor axis is 50 (nm). The constitutive relation of the water drop is modeled as a compressible Newtonian fluid,

$$\boldsymbol{\sigma} = \kappa(\ln J)\mathbf{I} + \mu(\nabla \otimes \mathbf{v} + (\nabla \otimes \mathbf{v})^T),$$

where $\mathbf{v}$ is the velocity of water, $J = \rho_0/\rho$, and ρ_0, ρ are the water density in the reference configuration and the current configuration. The bulk modulus and the viscosity of water are chosen as $\kappa = 2.2$ (GPa) and $\mu = 0.6$ (MPa s). The ambient space is modeled as the air, and the surface energy of water–air interface is $\gamma = 72.75$ (MN/m) (see [46]).

Fig. 22 shows the time sequences of the radial distances between the center of the water drop and the points A and B on the surface of a water droplet as shown in Fig. 21 by prescribing the surface tension based on analytical solution of Young's equation, which we refer to as *The Surface Traction Method*, and by using the proposed multiscale FEM dynamic wetting model, which we refer as *The Proposed Method*. One may find that first as time increases the radial coordinates of point A and point B become the same, i.e. the original ellipse becomes a circle. This makes sense because the surface of a liquid drop

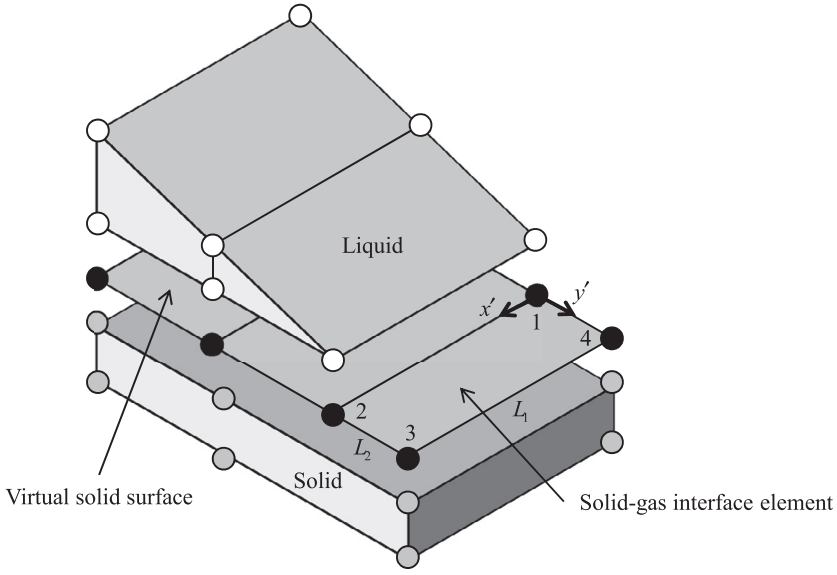

Fig. 20. The solid–gas interface element in three dimensional simulation.

tends to contract in order to attain the smallest possible surface area, and a sphere (in 2D a circle) has the smallest surface area for a given volume [42]. This ellipse to circle deformation process is displayed in Fig. 23, and the simulation is conducted by using the proposed discrete surface tension method. A same numerical simulation is conducted for a suspended 3D water droplet, in which we apply surface tension the surface of an ellipsoidal by using the proposed method. Under the action of the surface tension, the ellipsoid becomes a sphere (see Fig. 4). Moreover, from Fig. 22, one may find that the proposed discrete surface tension method provides the exact same results as that by using the analytical surface traction method, which validates the discrete surface tension method. The same validation is also performed in three dimensional case, in which the surface tension is applied to a water drop with initial ellipsoidal shape by using the discrete surface tension method. Fig. 24 shows the deformation time sequence in which an ellipsoid becomes a sphere under the prescribed surface tension by using the proposed discrete surface tension method.

7.2. Capillary rise

In this example, we simulate the capillary rise and compare the simulation result with the analytical result. The analytical solution of the capillary rise in a tube is known as the solution of the Lucas–Washburn equation [27,49], which can be expressed in the following expression,

$$h(t) = \sqrt{\frac{R\gamma\cos\theta}{2\mu}t}, \tag{100}$$

where $h(t)$ is the equilibrium height, R is radius of a tube, γ is surface tension between the liquid and gas, θ is contact angle, μ is dynamic viscosity of the liquid, and $t$is time.

The analytical solution for the equilibrium height for a 2D channel is

$$h(t) = \sqrt{\frac{2R\gamma\cos\theta}{3\mu}t} \tag{101}$$

and the equilibrium height is also proportional to square root of time (see Fig 25).

In this section, a two-dimensional simulation is performed, and it is compared with the analytical solution Eq. (101). The finite element model of capillary rise is shown in Fig. 26, in which the symmetric condition is used in computations. The distance between two walls is $2R = 8$ (nm), surface energy between the liquid and gas is $\gamma = 72.75$ (MN/m), contact angle is $\theta = 50^{\circ}$, dynamic viscosity is $\mu = 1$ (MPa s), and the solid is considered to be a rigid body. The body-surface interaction method of the Coarse Grained Contact Model is applied to the interaction between the liquid and solid.

When the Coarse Grained Contact Model is used in simulation, there is a gap between two contacting bodies. To check whether or not a node of liquid surface node is in contact with the solid surface, the following contact detection algorithm is applied in the computation: In the case of two dimensional simulations, the solid surface equation may be represented as a linear equation $ax + by + c = 0$, where $a,\ b$ and c are constant coefficients, and the liquid node is defined as $\mathbf{x}_0 = (x_0, y_0)$, thus, the distance between the liquid node and solid surface D is given by

$$D = \frac{|\, ax_0 + by_0 + c \,|}{\sqrt{a^2 + b^2}}. \tag{102}$$

In three dimensional computations, the solid surface equation is described by $ax + by + cz + d = 0$, where $a,\ b,\ c$ and d are constant coefficients, and the liquid node is $\mathbf{x}_0 = (x_0, y_0, z_0)$, and thus, the distance between the liquid node and solid surface D is given by

$$D = \frac{|\, ax_0 + by_0 + cz_0 + d \,|}{\sqrt{a^2 + b^2 + c^2}}. \tag{103}$$

If $D < \epsilon$, where ϵ is the contact tolerance, the liquid node is in contact with the solid surface.

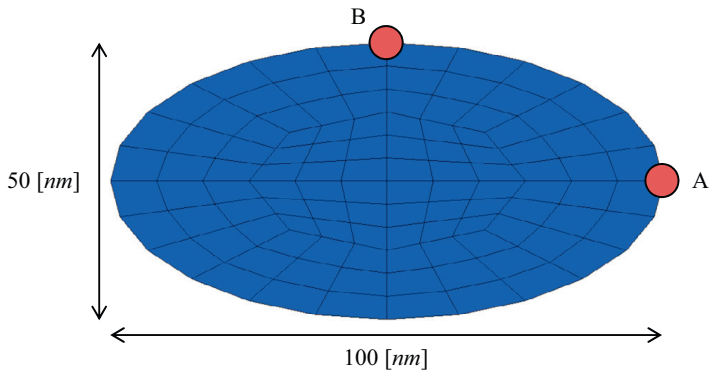

Fig. 21. Two dimensional model of water drop under surface tension.

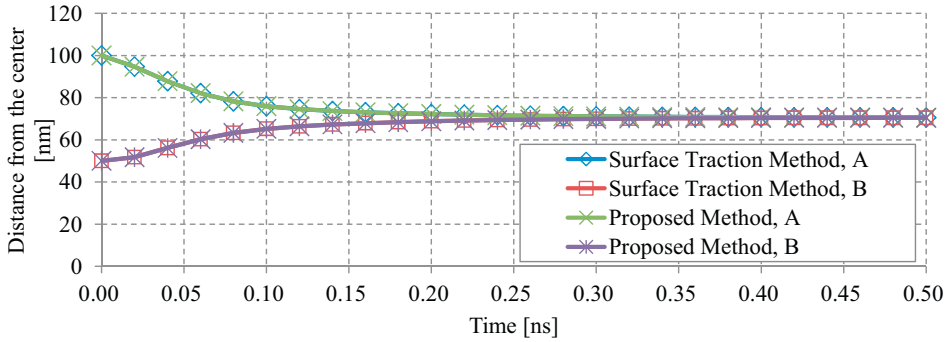

Fig. 22. The radial coordinates of points A and B calculated by using the surface traction method and the proposed surface tension method.

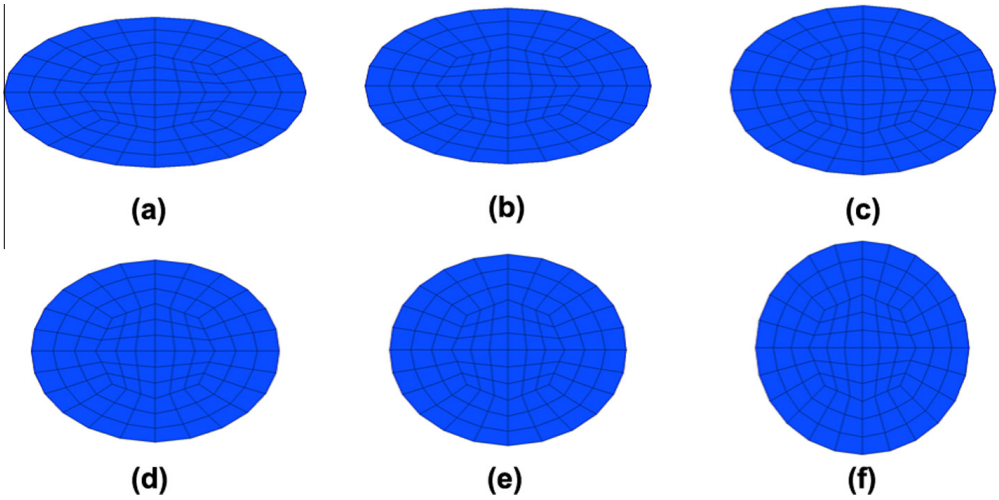

Fig. 23. Deformation of an ellipse due to the surface tension: (a) 0 (ns), (b) 20 (ns), (c) 40 (ns), (d) 60 (ns), (e) 80 (ns), (f) 500 (ns).

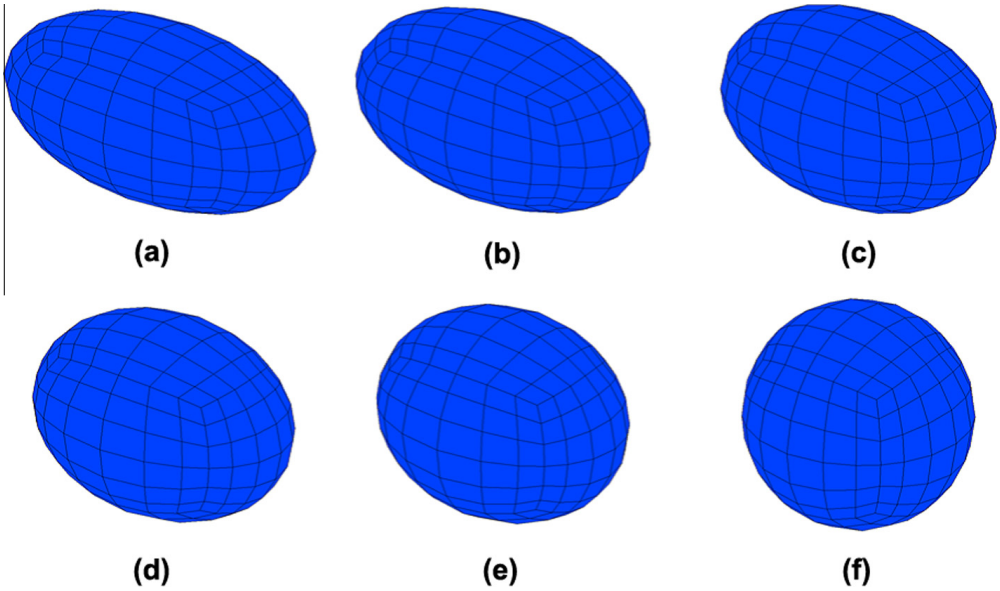

Fig. 24. Deformation of an ellipsoid due to the surface tension: (a) 0 (ns), (b) 20 (ns), (c) 40 (ns), (d) 60 (ns), (e) 80 (ns), (f) 500 (ns).

The comparison between the analytical solution and the numerical solution of the equilibrium height is shown in Fig. 27.

In Fig. 27, the method 1 and 2 refer to the two different FEM implementations: (1) FEM implementation based on Eq. (51) and (2) FEM implementation based on Eq. (52).

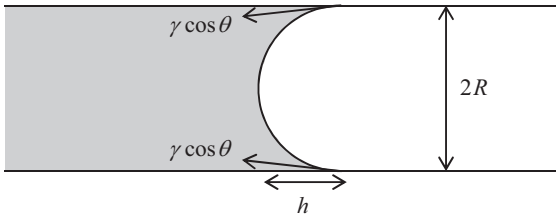

Fig. 25. Capillary rise between two walls.

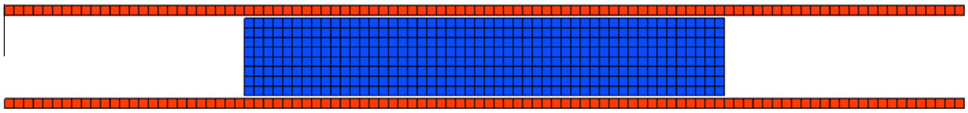

Fig. 26. FEM model of the capillary rise.

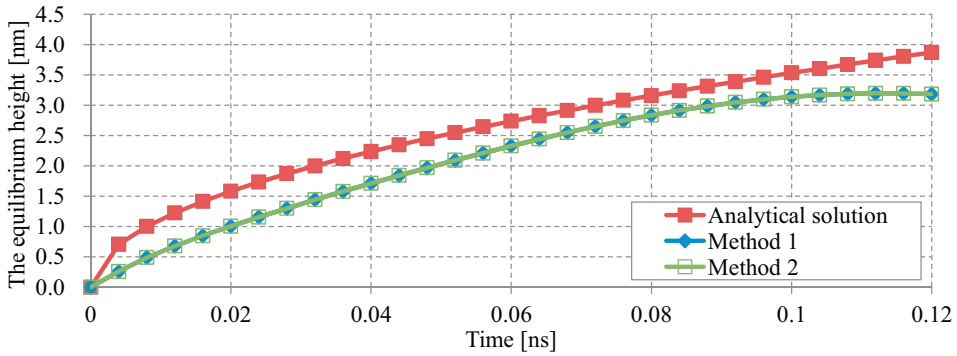

Fig. 27. The analytical solution and numerical simulation result of the equilibrium height.

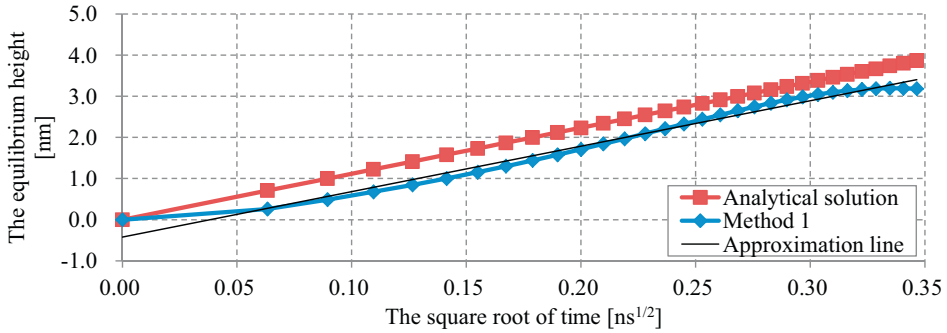

Fig. 28. The relationship between the equilibrium height and $\sqrt{t}$.

Both method 1 and 2 yield almost the same results, but they are different from the analytical solution at the beginning of the simulation. The analytical solution, Eq. (101), assumes the constant contact angle during the capillary rise, and this is the reason why the equilibrium height of the analytical solution sharply rises at the beginning of the simulation. On the other hand, the contact angle in dynamic wetting changes with time during the actual physical event, as well as in the virtual simulation by using the proposed dynamic wetting model. Because of these differences, the analytical solution and the numerical solution obtained in computations are different at the beginning of the simulation. Furthermore, the equilibrium height of the analytical solution keeps increasing because the equilibrium height is simply proportional to square root of time (see Eq. (101)). On the other hand, our simulation shows that the simulated equilibrium height of the proposed method is saturated after 0.1 (ns).

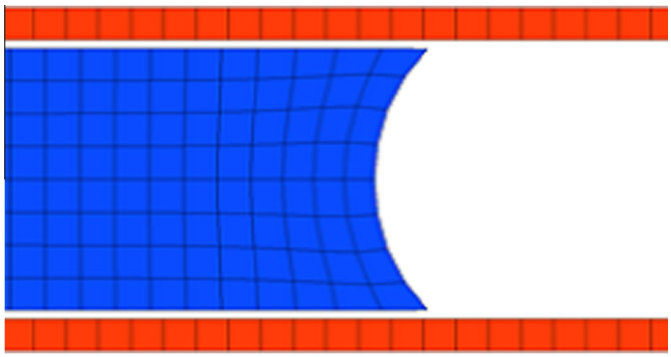

Fig. 29. The deformation of the capillary rise at 0.1 (ns).

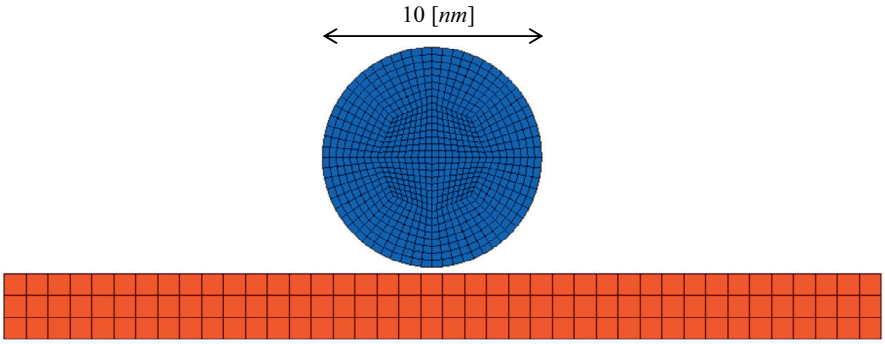

Fig. 30. FEM simulation model for droplet spreading in two dimension.

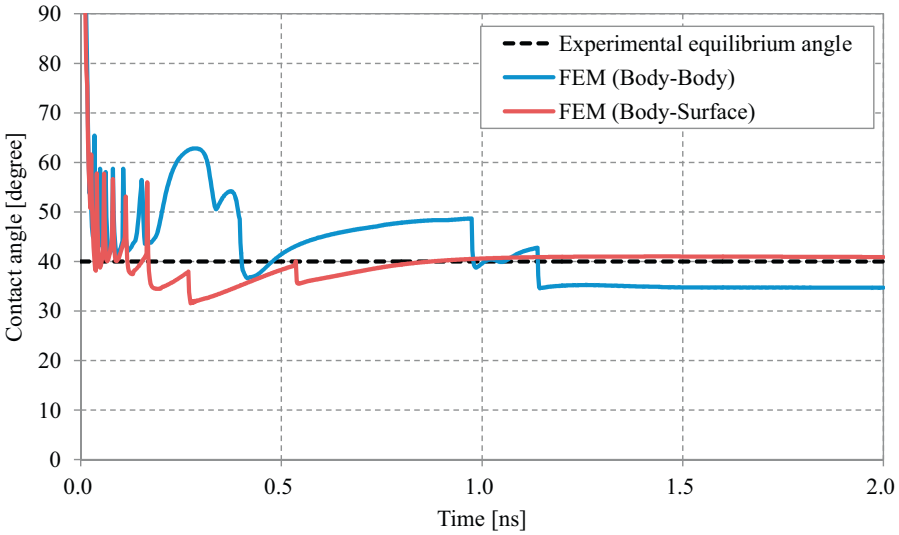

Fig. 31. The comparison of the contact angles between numerical results and experimental data.

Fig. 28 shows the relationship between the equilibrium height and the square root of time. The factor of proportionality of analytical solution is 11.167 $(\mathrm{nm}/\sqrt{\mathrm{ns}})$, and the slope of the approximation line of the numerical simulation result is 11.035; $(\mathrm{nm}/\sqrt{\mathrm{ns}})$. Hence, it is fair to say the result obtained from the proposed dynamic wetting model is in good agreement with the analytical solution, especially in middle section the simulation. The deformed liquid column at the time 0.1 (ns) is shown in Fig. 29.

7.3. Droplet spreading

In this example, we report the simulation of droplet spreading by using the proposed MDWM method. In this example, the liquid phase is a water droplet, and it is modeled as a Newtonian fluid. The solid phase is chosen as a single crystal copper

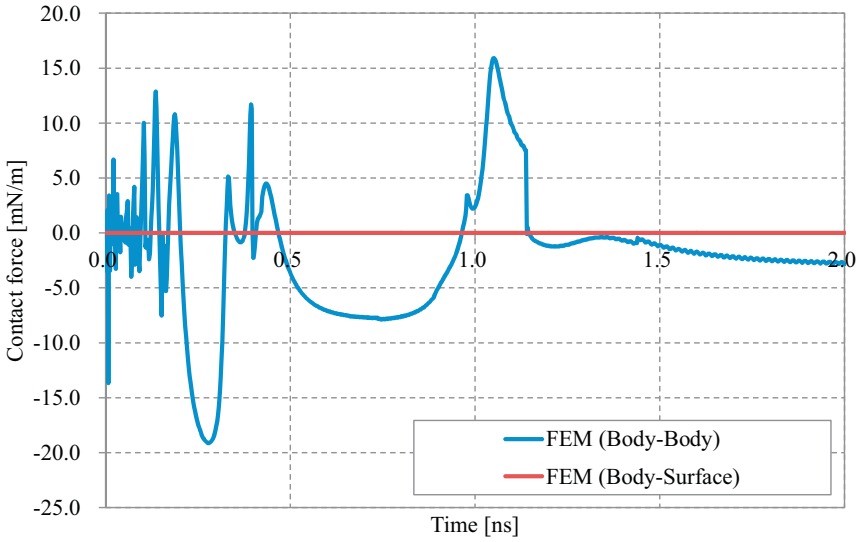

Fig. 32. The contact force in the parallel direction of the solid surface at the contact line.

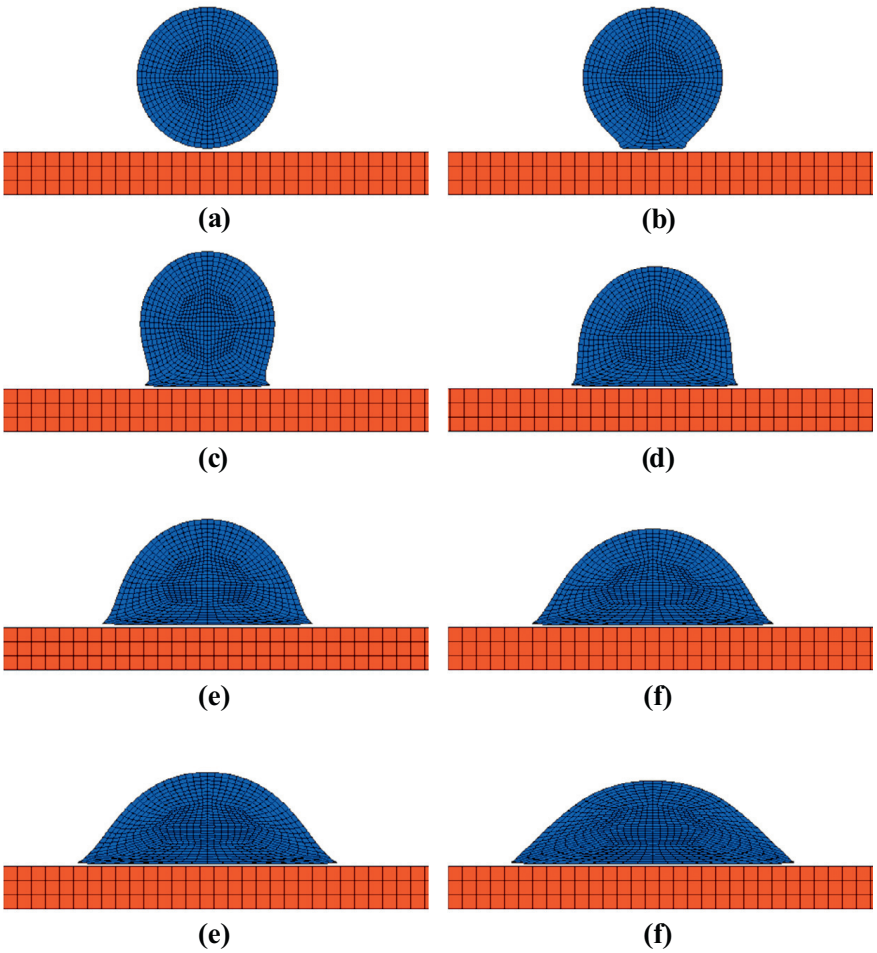

Fig. 33. The deformation: (a) 0 (ns), (b) 0.01 (ns), (c) 0.03 (ns), (d) 0.06 (ns), (e) 0.10 (ns), (f) 0.15 (ns), (g) 0.20 (ns), (h) 1.00 (ns).

substrate, whose material properties, including surface energy and surface tension, are derived by an atomistic potential in combination of the surface Cauchy–Born rule. In specific, we adopt the EAM-Holian potential in the computation [19,47]. Last the gas phase is chosen as air. A two-dimensional FEM droplet/substrate model is shown in Fig. 30. There is no FEM discretization for ambient air environment.

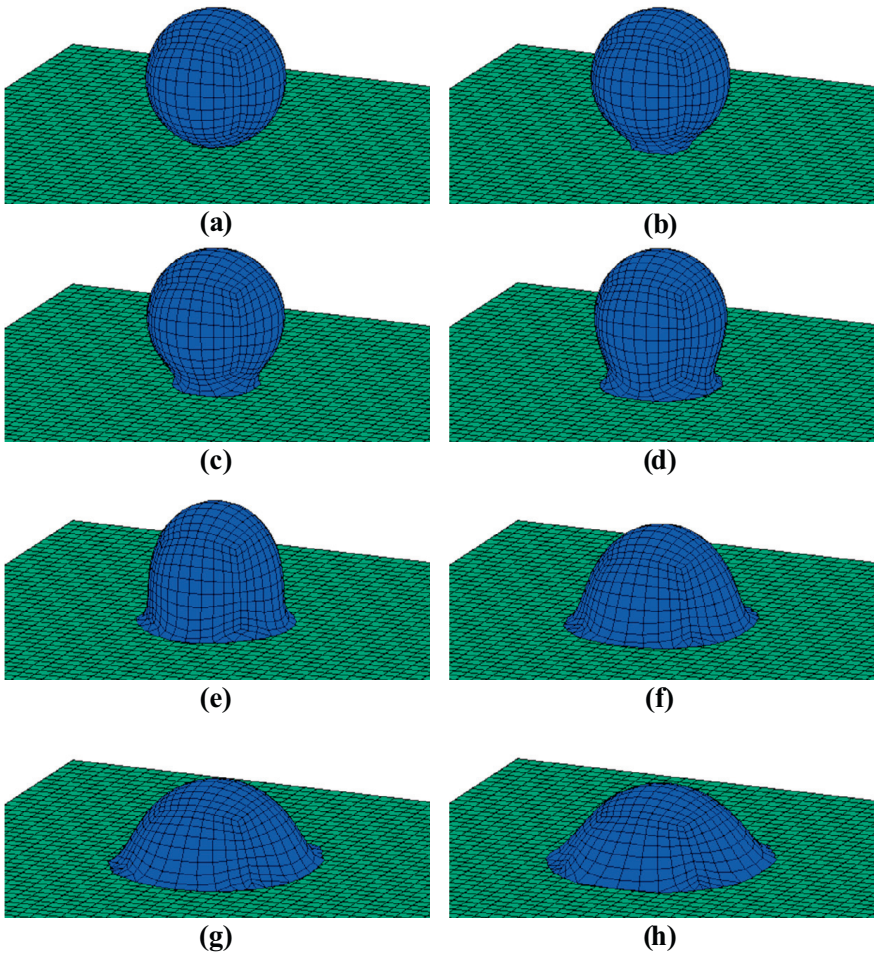

Fig. 34. The deformation: (a) 0 (ns), (b) 0.005 (ns), (c) 0.01 (ns), (d) 0.02 (ns), (e) 0.04 (ns), (f) 0.06 (ns), (g) 0.08 (ns), (h) 0.10 (ns).

In this triple system, the bulk modulus and the viscosity of water are given as $\kappa = 2.2$ (GPa) and $\mu = 0.6$ (MPa s). The surface energy between the water and air is $\gamma_{LG} = 72.75$ (MN/m) [46], the surface energy between the copper and air is $\gamma_{SG} = 1780$ (MN/m) [45]. The surface energy between the water and copper is derived from the Young equation and the experimental contact angle which is about 40° [24],

$$\gamma_{LS} = 1780 - 72.75 \cos 40 = 1724 \text{ (MN/m)}. \tag{104}$$

The material parameters of EAM-Holian/Cauchy–Born rule are listed in Appendix.

The parameters of Lennard–Jones potential used in the Coarse Grained Contact Model are computed from the arithmetic and geometric mean of the parameters from the pure water (w) and pure copper (c):

$$\epsilon^{cw} = \sqrt{\epsilon^c \epsilon^w} \tag{105}$$

and

$$r_0^{cw} = \frac{1}{2}(r_0^c + r_0^w). \tag{106}$$

The parameters of Lennard–Jones potential for water are obtained from [3], $\epsilon^w = 0.0067$ (eV) and $r_0^w = 0.355$ (nm). The parameters of Lennard–Jones potential for copper are $\epsilon^c = 0.073$ (eV) and $r_0^c = 0.260$ (nm). Hence, from these equation, $\epsilon^{cw} = 0.022$ (eV) and $r_0^{cw} = 0.3075$ (nm).

The history of dynamic contact angle is shown in Fig. 31. In this figure, the experimental contact angle is the equilibrium contact angle. FEM calculation results fluctuate, this is because that the liquid element makes contact with the solid surface one at time along the contact line in the spreading front, which causes numerical fluctuation. The numerical results also depend on the integration techniques used in the coarse-grain contact model (CGCM). The readers may find the detailed discussions on the body-to-body and the body-to-surface integrations in [32].

To calculate adhesive interaction of two bodies, we use either the body-to-body integration technique or the body-to-surface integration technique introduced in CGCM [38–41]. If we use the body-surface interaction method in simulations, the

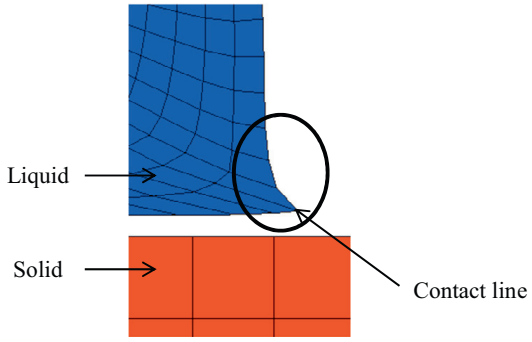

Fig. 35. The simulated dynamic contact angle.

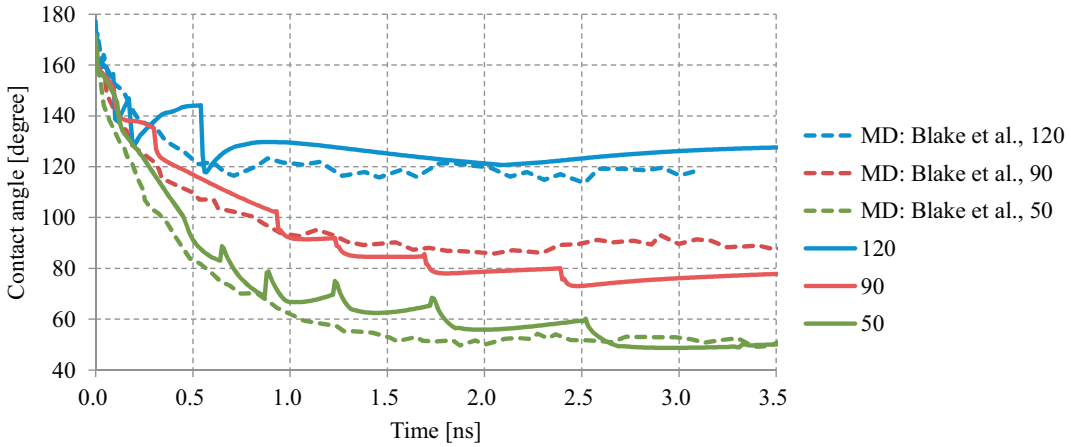

Fig. 36. The dynamic contact angle.

Table 1
The material parameters of EAM-Holian. The experimental date are obtained from [5].

	Parameter	Experiment	EAM-Holian
Cu	C_{1111} (GPa)	169	168.2
	C_{1122} (GPa)	122	117.5
	C_{1212} (GPa)	75.3	83.2
	ϵ (eV)		0.43894774
	r_0 (Å)		2.57110688
Ag	C_{1111} (GPa)	123	121.0
	C_{1122} (GPa)	92	84.5
	C_{1212} (GPa)	45.3	59.8
	ϵ (eV)		0.45921505
	r_0 (Å)		2.91297151
Al	C_{1111} (GPa)	108	95.4
	C_{1122} (GPa)	62	66.7
	C_{1212} (GPa)	28.3	47.2
	ϵ (eV)		0.35153936
	r_0 (Å)		2.88448279
Au	C_{1111} (GPa)	190	186.7
	C_{1122} (GPa)	161	130.4
	C_{1212} (GPa)	42.3	92.3
	ϵ (eV)		0.70311064
	r_0 (Å)		2.90584933
Ni	C_{1111} (GPa)	247	239.1
	C_{1122} (GPa)	153	167.0
	C_{1212} (GPa)	122	119.2
	ϵ (eV)		0.58932496
	r_0 (Å)		2.47623650

dynamic contact angle converges to 41°, which is almost the same as the experimental contact angle. On the other hand, if we use the body-body integration method, the dynamic contact angle converges to 35°. Fig. 32 shows that the contact force is in the parallel direction of the solid surface at the contact line. Since copper is much stiffer than water, the deformation of the copper substrate is almost negligible. Moreover since the solid surface is large enough, the contact force in the horizontal direction must be zero. Indeed, the body-surface interaction method shows zero horizontal force, but the body-body interaction method shows large horizontal force compared to the value of surface energy. Due to the existence of this imbalance force, the contact angle of the body-body interaction method may converge to a different angle from that observed in the experiment. A time sequence of the 2D water droplet spreading is shown in Fig. 33.

In addition to the two dimensional analysis, three dimensional simulations have also been performed. The simulation conditions of three dimensional analysis are exactly the same as that of the two dimensional analysis. The spreading sequence of the water drop are shown in Fig. 34.

Second, the proposed MDWM method is also tested against with Molecular Dynamics simulation of droplet spreading reported by Blake et al. [4]. The simulation model is the same as that shown in Fig. 30. The liquid is assumed to be hexadecane, and the parameters of Lennard–Jones potential between the liquid and solid are chosen as: $\epsilon^{ls} = 0.0259$ (eV) and $r_0^{ls} = 0.39$ (nm). The viscosity of the liquid is: $\mu = 5.82$ (MPa s), and the surface energy between the liquid and gas is chosen as: 27.5 (MN/m), which are obtained based on the data of molecular dynamics simulation. In the MD simulation [15], the material of the solid phase is not specified. However by analyzing the MD simulation results, we find that the interface energy between the solid substrate and the air is close to that of copper/air interphase, $\gamma_{SG} = 1780$ (MN/m) [45]. In this triple system, the equilibrium contact angle is 120°, the surface energy between the liquid and gas is $\gamma_{LS} = 1794.25$ (MN/m) which can be estimated from the Young equation. Similarly, if the equilibrium contact angle changes to 90° or 50°, the surface energy between the liquid and gas will change to $\gamma_{LS} = 1780$ (MN/m) and $\gamma_{LS} = 1761.68$ (MN/m) respectively.

In this simulation, the contact angle is defined as the average angle of three elements along the contact line as shown in Fig. 35. The dynamic contact angle history obtained by using the proposed method is displayed in Fig. 36. Although the results obtained via the proposed method fluctuate due to the discrete nature of finite element method, the dynamic contact angle of the proposed method are in general agreement with the result obtained by using Molecular Dynamics.

8. Discussions

In this work we have presented, derived and studied a multiscale dynamic wetting model at mesoscale or maybe even macroscale level. The proposed multiscale dynamic wetting model is a nonlinear continuum model with featured capacities such as describing surface energy and surface tension, modeling adhesive contact, and capturing large and finite deformation.

The heart of the proposed MDWM model is the admixture of the coarse-grained contact model (CGCM) and the finite element based contact line theory. Because of this combination, the colloidal repulsive force levitates or separates the liquid phase from the solid substrate, which effectively eliminates the singularity problem that has been plagued with in the conventional contact line theory for many years. It is this advantage that allows us to simulate dynamic wetting phenomena such as droplet spreading, capillary rise, and more at continuum scale.

Two different implementations of the surface stress algorithm are discussed in this paper. We have implemented the method to simulated both capillary rise and droplet spreading problems in both two-dimensional and three-dimensional spaces. The results of the numerical simulations are in general agreement with either the analytical, experimental, or molecular dynamics simulation results.

The proposed multiscale dynamic wetting model can be naturally extended as a general theoretical and computational framework that incorporates the surface Cauchy–Born model based surface continuum mechanics theory instead of using the phenomenological Gurtin–Murdoch theory, which will be discussed in the future work.

Acknowledgments

The authors would like to thank Professor Tarek Zohdi of the University of California-Berkeley for his interests in this research. Dr. H. Minaki would like to thank the Bridgestone Co. for a graduate fellowship. The authors would like to thank an anonymous reviewer who provides many suggestions on improving the quality of the manuscript.

Appendix A. The Embedded Atom Method: Holian et al. Model

In this section, the Embedded Atom Method developed by Holian et al. [19,47,20] is introduced. This method is called EAM-Holian in this dissertation.

The pairwise interaction function has the cutoff form,

$$\phi(r) = \begin{cases} \chi\psi(r) & r < r_{spl}, \\ \chi\left\{\psi(r_{spl}) + \frac{\partial\psi}{\partial r}(r_{spl})(r - r_{spl}) - \frac{1}{6}A(r - r_{spl})^3\right\} & r_{spl} \leqslant r < r_{max}, \\ 0 & r_{max} \leqslant r, \end{cases}$$

where χ is a weighting parameter between zero and one, the parameter value $\chi = 1/3$ is taken for the Embedded Atom Method, r_{spl} is the inflection point in the potential, r_{max} is the cutoff distance,

$$\psi(r) = \epsilon\left\{\left(\frac{r_0}{r}\right)^{12} - 2\left(\frac{r_0}{r}\right)^{6}\right\}$$

and

$$A = \frac{8\left(\frac{\partial\psi}{\partial r}(r_{spl})\right)^3}{9\left(\psi(r_{spl})\right)^2},$$

where ϵ is the depth of the potential well, r_0 is the equilibrium distance. The inflection point r_{spl} can be obtained by

$$\frac{\partial^2\psi}{\partial r^2}(r_{spl}) = 0$$

and the value is $r_{spl} = 1.244455 r_0$. The cutoff distance is given by

$$r_{max} = r_{spl} - \frac{3\psi(r_{spl})}{2\frac{\partial\psi}{\partial r}(r_{spl})}$$

and the value is $r_{max} = 1.547537 r_0$. For $r < r_{spl}$, the pairwise interaction function is the exactly same as the Lennard–Jones potential, and the intermediate-range cubic spline [20] for $r_{spl} \leqslant r \leqslant r_{max}$. The derivative of the pairwise interaction function is

$$\phi(r) = \begin{cases} \chi\frac{\partial\psi}{\partial r}(r) & r < r_{spl}, \\ \chi\left\{\frac{\partial\psi}{\partial r}(r_{spl}) - \frac{1}{2}A(r - r_{spl})^2\right\} & r_{spl} \leqslant r < r_{max}, \\ 0 & r_{max} \leqslant r, \end{cases}$$

where

$$\frac{\partial\psi}{\partial r}(r) = -12\frac{\epsilon}{r}\left\{\left(\frac{r_0}{r}\right)^{12} - \left(\frac{r_0}{r}\right)^{6}\right\}.$$

The electron density function is given by

$$\rho(r) = \begin{cases} \frac{1}{d(d+1)}\left(\frac{r_{max}^2 - r^2}{r_{max}^2 - r_0^2}\right)^2 & r < r_{max}, \\ 0 & r_{max} \leqslant r, \end{cases}$$

where $d$is the dimensionality. The derivative of the electron density is given by

$$\frac{\partial\rho}{\partial r}(r) = \begin{cases} -\frac{4}{d(d+1)}\frac{r\left(r_{max}^2 - r^2\right)}{\left(r_{max}^2 - r_0^2\right)^2} & r < r_{max}, \\ 0 & r_{max} \leqslant r. \end{cases}$$

The embedding energy function is chosen to be a nonlinear function of the form,

$$F(\rho) = (1 - \chi)\epsilon\frac{d(d+1)}{2}e\rho\ln\rho,$$

where e is the base of the natural logarithms. Clearly, at normal density, where the local embedding energy is $\rho = 1/e$, the embedding energy contributes a fraction $1 - \chi$ to the total cohesive energy. The derivative of the embedding energy function is given by

$$\frac{\partial F}{\partial\rho}(\rho) = (1 - \chi)\epsilon\frac{d(d+1)}{2}e(\ln\rho + 1).$$

Finally, there are only two material parameters, the depth of the potential well ϵ and the equilibrium distance r_0. These parameters are not shown in references and are obtained by following way in this dissertation. First, the equilibrium distance r_0 is determined as $\boldsymbol{\sigma} = \mathbf{0}$ when there is no deformation, $\mathbf{F} = \mathbf{I}$. The Cauchy stress is computed from the Cauchy–Born rule. In this calculation, ϵ is taken to be unity, $\epsilon = 1$, and up to the third nearest neighbors on FCC lattice are considered. Second, the depth of the potential well ϵ is obtained by least squares method,

$$\left(C_{1111}^{exp} - \epsilon C_{1111}^{CB}\right)^2 + \left(C_{1122}^{exp} - \epsilon C_{1122}^{CB}\right)^2 + \left(C_{1212}^{exp} - \epsilon C_{1212}^{CB}\right)^2 = Min,$$

where C_{1111}^{exp}, C_{112}^{exp} and C_{1212}^{exp} are the experimental values, and C_{1111}^{CB}, C_{112}^{CB} and C_{1212}^{CB} are obtained from the Cauchy–Born rule. By taking the derivative with respect to ϵ, we have

$$\epsilon = \frac{C^{exp}_{1111}C^{CB}_{1111} + C^{exp}_{1122}C^{CB}_{1122} + C^{exp}_{1212}C^{CB}_{1212}}{\left(C^{CB}_{1111}\right)^2 + \left(C^{CB}_{1122}\right)^2 + \left(C^{CB}_{1212}\right)^2}.$$

Table 1 shows the fitting results and the material parameters. The experimental data are taken from [5].

References

[1] T. Belytschko, W.K. Liu, B. Moran, Nonlinear Finite Elements for Continua and Structures, John Wiley & Sons Ltd., Baffins Lane, Chichester, West Sussex, England, 2000.
[2] J.U. Brackbill, D.B. Kothe, C. Zemach, A continuum method for modeling surface tension, J. Comput. Phys. 100 (1992) 335–354.
[3] H.J.C. Berendsen, J.R. Grigera, T.P. Straatsma, The missing term in effective pair potentials, J. Phys. Chem. 91 (1987) 6269–6271.
[4] T.D. Blake, A. Clarke, J. de Coninck, M. de Ruijter, M. Voue, Droplet spreading: a microscopic approach, Colloids Surf. A: Physicochem. Eng. Aspects 103 (1999) 123–130.
[5] M.M. Choy, W.R. Cook, R.F.S. Hearmon, J. Jaff, J. Jerphagnon, S.K. Kurtz, S.T. Liu, D.F. Nelson, Elastic, Piezoelectric, Pyroelectric, Piezooptic, Electrooptic Constants, and Nonlinear Dielectric Susceptibilities of Crystals, Springer-Verlag, Berlin, 1971.
[6] B.V. Derjaguin, Friction and adhesion. IV. The theory of adhesion of small particles, Kolloid Z. 69 (1934) 155–164.
[7] A. Jagota, C. Argento, An intersurface stress tensor, J. Colloid Interface Sci. 191 (1997) 326–336.
[8] B.V. Derjaguin, V.M. Muller, Y.P. Toporov, Effect of contact deformation on the adhesion of particles, J. Colloid Interface Sci. 53 (1975) 314–326.
[9] E.B. Dussan V., S.H. Davis, On the motion of a fluid–fluid interface along a solid surface, J. Fluid Mech. 65 (1974) 71–95.
[10] E.B. Dussan V., The moving contact line: the slip boundary condition, J. Fluid Mech. 77 (1976) 665–684.
[11] E.B. Dussan V., On the spreading of liquids on solid surfaces: static and dynamics contact lines, Annu. Rev. Fluid Mech. 11 (1979) 371–400.
[12] P.G. de Gennes, Wetting: statics and dynamics, Rev. Mod. Phys. 57 (1985) 827–863.
[13] Z.G. Feng, M. Domaszewski, G. Montavon, C. Coddet, Finite element analysis of effect of substrate surface roughness on liquid droplet impact and flattening process, J. Therm. Spray Technol. II (2002) 62–68.
[14] J. Fukai, Z. Zhao, D. Poulikakos, C.M. Megaridis, O. Miyatake, Modeling of the deformation of a liquid droplet impinging upon a flat surface, Phys. Fluids 5 (1993) 2588–2599.
[15] M.J. de Ruijter, T.D. Blake, J. de Coninck, Dynamic wetting studied by molecular modeling simulations of droplet spreadint, Langmuuir 15 (1999) 7836–7847.
[16] M.E. Gurtin, A.I. Murdoch, A continuum theory of elastic material surfaces, Arch. Ration. Mech. Anal. 57 (1975) 291–323.
[17] M.E. Gurtin, A.I. Murdoch, Surface stress in solids, Int. J. Solids Struct. 14 (1978) 431–440.
[18] M.E. Gurtin, J. Weissmuller, F. Larche, A general theory of curved deformable interfaces in solids at equilibrium, Philos. Mag. A 78 (1998) 1093–1109.
[19] B.L. Holian, A.F. Voter, N.J. Wagner, R.J. Ravelo, S.P. Chen, W.G. Hoover, C.G. Hoover, J.E. Hammerberg, T.D. Dontje, Effects of pairwise versus many-body forces on high-stress plastic deformation, Phys. Rev. A 43 (1991) 2655–2661.
[20] B.L. Holian, R. Ravelo, Fracture simulations using large-scale molecular dynamics, Phys. Rev. B 51 (1995) 11275–11288.
[21] T.J.R. Hughes, The Finite Element Method: Linear Static and Dynamic Finite Element Analysis, second ed., Dover Publications, Mineola, NY, 2000.
[22] C. Huh, L.E. Scriven, Hydrodynamic model of steady movement of a solid/liquid/fluid contact line, J. Colloid Interface Sci. 35 (1963) 85–101.
[23] K.L. Johnson, K. Kendall, A.D. Roberts, Surface energy and the contact of elastic solids, Proc. R. Soc. A 324 (1971) 301–313.
[24] S.G. Kandlikar, M.E. Teinke, Contact angles and interface behavior during rapid evaporation of liquid on a heated surface, Int. J. Heat Mass Transfer 45 (2002) 3771–3780.
[25] V.G. Levich, V.S. Krylov, Surface tension driven phenomena, Annu. Rev. Fluid Mech. 1 (1969) 293–316.
[26] S. Li, G. Wang, Introduction to Micromechanics and Nanomechanics, World Scientific Publishing Company, Singapore, 2008.
[27] von R. Lucas, Ueber das Zeitgesetz des kapillaren Aufstiegs von Flussigkeiten, Kolloid-Zeitschrift 23 (1918) 15–22.
[28] S. Madasu, R.A. Cairncross, Effect of substrate flexibility on dynamic wetting: a finite element model, Comput. Methods Appl. Mech. Eng. 192 (2003) 2671–2702.
[29] S. Manservisi, R. Scardovelli, A variational approach to the contact angle dynamics of spreading droplets, Comput. Fluids 38 (2009) 406–424.
[30] A. Marchand, J.H. Weijs, J.H. Snoeijer, B. Andreotti, Why is surface tension a force parallel to the interface?, Am J. Phys. 10 (2011) 999–1008.
[31] J.E. Marsden, T.J.R. Hughes, Mathematical Foundations of Elasticity, Prentice Hall, Eaglewood Cliffs, NJ, 1983.
[32] H. Minaki, A multiscale analysis of dynamic wetting (Ph.D. dissertation), The University of California-Berkeley, 2013.
[33] H.K. Moffatt, Viscous and resistive eddies near a sharp corner, J. Fluid Mech. 18 (1963) 1–18.
[34] H.S. Park, P.A. Klein, G.J. Wagner, A surface Cauchy–Born model for nanoscale materials, Int. J. Numer. Methods Eng. 68 (2006) 1072–1095.
[35] H.S. Park, P.A. Klein, Surface stress effects on the resonant properties of metal nanowires: the importance of finite deformation kinematics and the impact of the residual surface stress, J. Mech. Phys. Solids 56 (2008) 3144–3166.
[36] J.M.H. Peters, Total curvature of surfaces (via the divergence of the normal), Int. J. Math. Edu. Sci. Technol. 32 (2001) 795–810.
[37] T. Qian, X.-P. Wang, P. Sheng, A variational approach to moving contact line hydrodynamics, J. Fluid Mech. 564 (2006) 333–360.
[38] R.A. Sauer, S. Li, A contact mechanics model for quasi-continua, Int. J. Numer. Methods Eng. 71 (2007) 931–962.
[39] R.A. Sauer, S. Li, An atomic interaction-based continuum model for adhesive contact mechanics, Finite Elem. Anal. Des. 43 (2007) 384–396.
[40] R.A. Sauer, S. Li, An atomiscically enriched continuum model for nanoscale contact mechanics and its application to contact scaling, J. Nanosci. Nanotechnol. 8 (2007) 1–17.
[41] R.A. Sauer, S. Li, An atomic interaction-based continuum model for computational multiscale contact mechanics, Proc. Appl. Math. Mech. (PAMM) 7 (2008) 4080029–4080030.
[42] A.J. Smits, A Physical Introduction to Fluid Mechanics, John Wiley & Sons, Inc., 2000.
[43] C.A. Truesdell, A First Course in Rational Continuum Mechanics, Academic Press, New York, San Francisco, London, 1976.
[44] C.A. Truesdell, W. Noll, The Non-Linear Field Theories of Mechanics, second ed., Springer-Verlag, 1992.
[45] W.R. Tyson, W.A. Miller, Surface free energies of solid metals estimation from liquid surface tension measurements, Surf. Sci. 62 (1977) 267–276.
[46] N.B. Vargaftik, B.N. Volkov, L.D. Voljak, International tables of the surface tension of water, J. Phys. Chem. Ref. Data 12 (1983) 817–820.
[47] N.J. Wagner, B.L. Holian, A.F. Voter, Molecular-dynamics simulations of two-dimensional materials at high strain rates, Phys. Rev. A 45 (1992) 8457–8470.
[48] X. Wang, X. Peng, D. Lee, Dynamic wetting and stress singularity on contact line, Sci. China 46 (2003) 407–417.
[49] E.W. Washburn, The dynamics of capillary flow, Phys. Rev. 17 (1921) 273–283.
[50] T. Young, An essay on the cohesion of fluids, Philos. Trans. R. Soc. 95 (1805) 65–87.
[51] Y.D. Shikhmurzaev, Singularities at the moving contact line. Mathematical, physical and computational aspects, Physica D 217 (2006) 121–133.
[52] O.C. Zienkiewicz, R.L. Taylor, J.Z. Zhu, Finite Element Method: Its Basis and Fundamentals, sixth ed., Elsevier, Oxford, Burlington, MA, 2005.